J. Fluid Mech. (2025), *vol.* 1025, A8, doi:10.1017/jfm.2025.10926

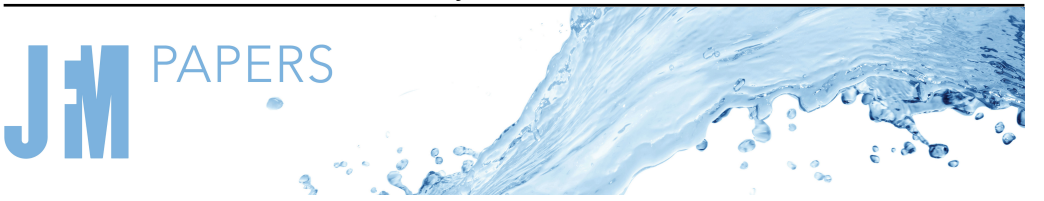

Coherent organisation of passive scalar from a point source in a turbulent boundary layer

Isaiah E. Wall[1] **and Gokul Pathikonda**[1]

[1]School for the Engineering of Matter, Transport and Energy (SEMTE), Arizona State University, Tempe, AZ, USA

Corresponding author: Gokul Pathikonda, gokul.pathikonda@asu.edu

(Received 10 April 2025; revised 5 August 2025; accepted 7 November 2025)

The spatial organisation of a passive scalar plume originating from a point source in a turbulent boundary layer is studied to understand its meandering characteristics. We focus shortly downstream of the isokinetic injection ($1.5 \leqslant x/\delta \leqslant 3$, δ being the boundary-layer thickness) where the scalar concentration is highly intermittent, the plume rapidly meanders and breaks up into concentrated scalar pockets due to the action of turbulent structures. Two injection locations were considered: the centre of the logarithmic region and the wake region of the boundary layer. Simultaneous quantitative acetone planar laser-induced fluorescence and particle image velocimetry were performed in a wind tunnel, to measure scalar mixture fraction and velocity fields. Single- and multi-point statistics were compared with established works to validate the diagnostic novelties. Additionally, the spatial characteristics of plume intermittency were quantified using 'blob' size, shape, orientation and mean concentration. It was observed that straining, breakup and spatial reorganisation were the primary plume-evolution modes in this region, with little small-scale homogenisation. Further, the dominant role of coherent vortex motions in plume meandering and breakup was evident. Their action is found to be the primary mechanism by which the injected scalar is transported away from the wall in high concentrations ('large meander events'). Strong spatial correlation was observed in both instantaneous and conditional fields between the high-concentration regions and individual vortex heads. This coherent transport was weaker for wake injection, where the plume only interacts with outer vortex motions. A coherent-structure-based mechanism is suggested to explain these transport mechanisms.

Key words: turbulent boundary layers, turbulent mixing, mass transport

1. Introduction

The evolution of a passive scalar plume in a turbulent boundary layer (TBL) is a problem of significant interest with direct implications to modelling and predicting pollutant transport, estimation of toxicity and flammability of accidental/intentional chemical releases, modelling odour nuisance, modelling atmospheric chemistries, source triangulation from discrete scalar measurements, etc. (Cassiani *et al.* 2020). For all of these applications, knowledge about the evolution of the concentration statistics (e.g. mean and probability density function (PDF)) and their relation to the turbulence field evolution is critical. For example, the ability to evaluate chronic effects of an anthropogenic scalar on a neighbourhood is strongly related to the ability to accurately estimate mean scalar concentration maps. On the other hand, the estimation of acute effects or flammability/explosivity limits of accidental releases requires a more detailed knowledge of the higher-order statistics (variance, level-crossing probability, etc.) or the concentration PDF. The evolution of all of these quantities in the real world is almost always coupled with atmospheric weather patterns and natural/urban topographies in a highly nonlinear and unsteady manner.

In the current study, we consider the canonical configuration where we focus on the evolution of a passive scalar injected isokinetically from a point source into a moderate-Reynolds-number (Re_τ) TBL that sustains prominent coherent structures (Robinson 1991; Adrian *et al.* 2000*b*; Adrian 2007). We suspect that capturing the interactions between the coherent structures and scalar plume is essential for developing a comprehensive phenomenological model that can account for rare events that deviate significantly from the mean (such as large meander, high concentration, etc.). Further, we limit our discussion and comparisons to laboratory experiments, and the reader is referred to Fernando *et al.* (2010) for an overview of field measurements made in real atmospheric flows.

1.1. *Overview of point-source scalar transport in boundary layers*

We can qualitatively describe the evolution of scalar plume injected in a TBL (outlined in figure 1) from a source with a size d_s. In the region immediately downstream ($x \lesssim 1\delta$, stage 1, δ being the boundary-layer thickness), the plume is characterised by clear continuous boundaries (demarking the scalar and the ambient fluid) and a homogeneous concentration that meanders due to the action of turbulent scales, $\lambda \gg d_s$. Subsequently, the plume stretches, strains and breaks up in the intermediate region ($1\delta \lesssim x \lesssim 10\delta$, stage 2) that is characterised by discrete parcels of scalar mixing in the TBL. As these parcels grow in wall-normal extent faster than the boundary-layer growth, they eventually create a continuous scalar field within the boundary layer (i.e. the boundary layer has approximately non-zero concentrations of marked scalar everywhere, stage 3). This entire process occurs under the influence of a range of turbulent eddies/vortices, and their effects on the plume depend on the relative size of the plume and the eddies within each stage. In other words, structures much larger than the plume predominantly cause the plume to meander, structures much smaller than the plume cause mixing within the plume/parcels and structures of the same order of the plume width tend to stretch and strain the plume (i.e. change the shape of the plume/parcels). The defining quantitative measure of the three evolution stages is the concentration intermittency factor, γ. At a given spatial region, it is defined as the fraction of time where a nonzero concentration of scalar is observed ($N_{c>0}/N$, where N is an instance of measurement). For example, along the injection line in the streamwise direction, γ starts at 100 % (where a scalar is always observed, stage 1), decreases to a minimum ($\approx$40 % in the region of highly intermittent flow, stage 2) and then

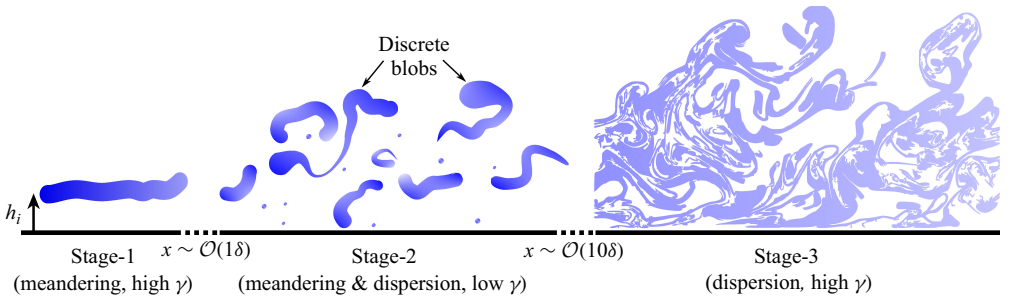

Figure 1. Schematic of different stages of plume evolution and dominant mechanisms (stage 3 representation based on image from Crimaldi & Koseff (2001)).

increases back to ≈100 % as the scalar is dispersed throughout the boundary layer (stage 3) (Fackrell & Robins 1982*a*,*b*; Sawford, Frost & Allan 1985) (Note that due to continuous entrainment of free-stream fluid, $\gamma < 100$ % strictly.) Thus, high intermittency (low γ) is a defining characteristic of the intermediate region ($x \approx 1\delta - 10\delta$).

The qualitative nature of the plume-spread in the different stages is a strong function of injection parameters, specifically source size d_s and the source injection height h_i within the boundary layer (Fackrell & Robins 1982*a*,*b*; Sawford & Hunt 1986). For a scalar injection very close to the wall ($h_i \approx 0$, known as 'ground-level source'), the viscous sublayer has a propensity to collect the scalar over an extended region and serve as a scalar reservoir to the rest of the boundary layer (Crimaldi, Wiley & Koseff 2002; Lim & Vanderwel 2023). In contrast, injection at higher elevations tends to spread through the entirety of the boundary layer at a much faster rate, due to the transverse plume growth rate being greater than the boundary layer growth rate (Poreh & Cermak 1964). Quantitatively, the evolution of mean scalar concentration from an elevated source is known to follow a self-similar, reflected Gaussian profile (discussed later in relation to (3.1)) (Fackrell & Robins 1982*b*; Yee *et al.* 1993*a*,*b*; Crimaldi & Koseff 2001; Crimaldi *et al.* 2002; Nironi *et al.* 2015; Talluru *et al.* 2017; Cassiani *et al.* 2024). However, deviations from this form are observed in the outer regions of the TBL (that has both turbulent and non-turbulent regions; Talluru *et al.* 2017) and very close to the wall (Yee *et al.* 1993*a*,*b*). Similar Gaussian form was shown to fit the evolution of the concentration variance within the boundary layer as well (Crimaldi & Koseff 2001; Crimaldi *et al.* 2002; Cassiani *et al.* 2024). Self-similarity of temporal scalar spectra was also observed in the spanwise–wall-normal plane when scaled by the outer scales (boundary-layer thickness δ and free-stream velocity U_∞; Talluru, Philip & Chauhan 2019).

While the trends for mean and variance of concentration describe the structure of average plume, the turbulent scalar transport mechanisms that result in said trends are captured by the turbulent fluxes ($\overline{u'c'}$, $\overline{v'c'}$, $\overline{w'c'}$), measuring of which requires simultaneous measurements of both concentration and velocity (here a prime represents fluctuations in velocity u, v, w and scalar concentration c). The streamwise and wall-normal turbulent fluxes ($\overline{u'c'}$ and $\overline{v'c'}$, respectively) display a characteristic 'S'-shape in their wall-normal variation with an inflection point at the injection height ($y = h_{inj}$). Turbulent flux, $\overline{v'c'}$ is positive above the injection height and negative below (Fackrell & Robins 1982*b*), consistent with the scalar transport away from h_i. Similar trends are also observed for spanwise turbulent flux $\overline{w'c'}$ in the spanwise direction at all heights. The steamwise turbulent flux $\overline{u'c'}$ shows the opposite sign to $\overline{v'c'}$ with an inflection point slightly below h_i for injection locations close to the wall (Talluru, Philip & Chauhan 2018).

This quantity, however, is not dynamically dominant, relative to cross-stream fluxes (i.e. $\overline{v'c'}$ and $\overline{w'c'}$) since advection due to mean velocity is significantly stronger than turbulent transport (Fackrell & Robins 1982*b*). Finally, in addition to these trends in single-point statistics, the spatial structure of the plume was quantified via two-point scalar correlation using planar measurements by Miller (2005) and synchronised two-probe measurements by Talluru & Chauhan (2020), who showed that the two-dimensional two-point scalar correlation map had an oval shape that tilts in the direction of the mean shear. The inclination angle was also found to increase with downstream distance (Miller 2005).

These early canonical plume transport studies were primarily directed at developing and validating novel analytical approaches and numerical schemes applicable to realistic scalar transport processes (Cassiani *et al.* 2020). Specifically, the ability to predict spatial evolution of the mean concentration and higher-order statistics is of interest. One of the earliest mechanistic models that described the evolution of a scalar plume was the 'meandering plume' model, first proposed by Gifford (1959). The model considers that the plume evolution can be phenomenologically described as the sum of two statistically independent processes: (1) the meandering of the plume caused by velocity structures asymptotically larger than the plume's width and (2) dispersion and mixing at the boundaries of the plume caused by turbulence structures smaller than the width of the plume. The model has limitations: namely it starts to break down close to the wall (due to strong mean shear invalidating the turbulence isotropy assumption), far from the source (due to unrestricted growth of the plume; Fackrell & Robins 1982*b*) and outside the fully turbulent region of the boundary layer $\gtrsim 0.6\delta$ (Marro *et al.* 2015; Talluru *et al.* 2018). However, in the intermediate regime (stage 2) the plume has been observed to follow the presumed meandering behaviour very well, with large eddies making the plume meander, small eddies causing mixing at the boundaries and eddies roughly the size of the plume causing it to break up, stretch and elongate (Yee *et al.* 1993*a*, 2003; Talluru *et al.* 2018). For this reason, variations to this approach, collectively known as 'fluctuating plume models', have been developed extensively (Cassiani *et al.* 2020). The meandering plume description was further quantified by Talluru *et al.* (2018) in explaining the variations in observed turbulent fluxes, concentration time scales and organisation of structures relative to the plume centreline. For regions far from the injection location, the action of turbulence on plume mixing is more amenable to analytical approaches such as empirical and semi-empirical modelling, Lagrangian stochastic modelling, etc. Additionally, numerical methods such as Reynolds-averaged Navier–Stokes and PDF models, and scale-resolving simulations such as large-eddy simulations and direct numerical simulations are also feasible, but at an increased computational effort. Marro *et al.* (2015), Marro *et al.* (2018), Cassiani *et al.* (2020) and Cassiani *et al.* (2024) summarise the state of the art of these numerical efforts. Since most of these models focus on estimating the statistical representations of the concentration fields (mostly PDF and higher-order moments of concentration) without explicitly considering the turbulent mechanics, we do not discuss these approaches in further detail. The numerical efforts investigating the turbulent structure of the transport processes are discussed in § 1.2.

Experimentally understanding the two- and three-dimensional structure of both scalar and velocity, and their interplay, requires multi-point measurements/correlations, either via arrays of probes, via flow-field measurements, or via scale-resolving numerical simulations. This is particularly important to understand the precise turbulent mechanisms that result in this transport. Planar laser-induced fluorescence (PLIF) is commonly implemented to capture scalar concentration fields in a plane, in either streamwise–wall-normal ($x-y$) plane (Crimaldi & Koseff 2001; Crimaldi *et al.* 2002; Liao & Cowen 2002; Lim & Vanderwel 2023), spanwise–wall-normal ($y-z$) plane (Crimaldi *et al.* 2002;

Vanderwel & Tavoularis 2016) or streamwise–spanwise ($x-z$) plane (Crimaldi *et al.* 2002; Connor, McHugh & Crimaldi 2018; Eisma *et al.* 2021). These studies confirmed the self-similar behaviour of concentration and fluctuation profiles in both water (Crimaldi *et al.* 2002; Lim & Vanderwel 2023) and air (Connor *et al.* 2018). Lastly, Liao & Cowen (2002) used particle image velocimetry (PIV) and LIF to characterise the turbulent structures responsible for the creation and evolution of filament structures in the intermediate downstream region observing high levels of intermittency far from the injection location for scalars with low molecular diffusivity.

1.2. *Coherent structures and scalar transport*

Beyond the single-point measures, understanding the role of coherent structures that populate the boundary-layer flow (Robinson 1991) in scalar transport requires capturing the scalar and turbulent velocity flow fields simultaneously. These coherent structures have a dynamically significant footprint (Adrian 2007), and a finite spatio-temporal coherence (i.e. they exist for a long enough time in the flow to impact the flow qualitatively). Prominent structures of interest are the quasi-streamwise vortices close to the wall, wall-attached hairpin vortices in the logarithmic region (Kline *et al.* 1967; Townsend 1976) and hairpin packets that form a coherent group of hairpin vortices (Adrian *et al.* 2000*b*; Adrian 2007). The role of near-wall quasi-streamwise vortices in scalar transport has not been extensively studied since they are dominant only over hydrodynamically smooth surfaces, with limited relevance to atmospheric flows (that are typically 'fully rough'). On the other hand, hairpin vortices and hairpin packets populate the outer regions of a high-Re_τ ($\gtrsim 1000$) boundary layer over both smooth and rough surfaces (Volino, Schultz & Flack 2007; Wu & Christensen 2007). The term 'hairpin vortex' here will encompass all similar structured (hairpin, horseshoe, omega) vortices and their asymmetric and/or incomplete counterparts. They were first theorised by Theodorsen (1952), and their dynamical significance has been increasingly evident in recent times in creating large regions of roughly uniform momentum, generation of turbulent kinetic energy in the outer regions, transporting the near-wall turbulence via intense bursting events, etc. (Townsend 1976; Robinson 1991; Adrian *et al.* 2000*b*; Christensen & Adrian 2001; Ganapathisubramani *et al.* 2003, 2005; Natrajan & Christensen 2006; Adrian 2007). Further, these structures are dynamically dominant only at high-Re_τ conditions (i.e. $Re_\tau \gtrsim 1000$).

Efforts to study the role of these large structures in scalar transport are relatively recent. Vanderwel & Tavoularis (2016) conducted stereo-PIV and PLIF in a plane shear flow (without solid boundaries) and, using conditional averages, identified the structure of scalar transport by individual hairpin-type vortices. They found that both upright and inverted hairpin vortices preferentially oriented the scalar at angles of 155° and −25° with respect to the flow direction, which correlates with ejection/sweep events of the respectively aligned hairpin vortices (unlike plane shear flows, TBLs have almost exclusively upright hairpin vortices). This is similar to the subfilter-scale turbulent energy transfer and scattering events observed in boundary layers (Yee *et al.* 1993*a*; Natrajan & Christensen 2006). Following this, Talluru *et al.* (2017, 2018) performed two-probe simultaneous measurements within a high-Re_τ boundary layer and found preferential organisation of the coherent structures relative to the plume structure and the presence of low- and high-speed structures above and below the plume respectively. The researchers expanded on these observations in their subsequent works (Talluru *et al.* 2019; Talluru & Chauhan 2020) to investigate the structural inclination angle, self-similarity in temporal spectra and noticed a strong outer-layer scaling. They schematically provided a representative arrangement between momentum and scalar plume. Finally, a recent

investigation by Eisma *et al.* (2021) using high-speed, simultaneous measurements of scalar plume (in a plane using PLIF) and turbulent velocity field (in a volume, using volumetric PIV) identified the existence of uniform concentration zones similar to that of uniform momentum zones (UMZs) sustained by the hairpin vortex packets (Adrian 2007). Additionally, Lagrangian analysis using finite-time Lyapunov exponents identified a strong correlation with the uniform concentration zone boundaries. These measurements correspond to downstream sections away from the injection location where the plume already occupies a significant portion of the boundary layer (i.e. stage 3 in figure 1). Finally, even though not directly investigating a passive scalar from a point source, Dharmarathne *et al.* (2016), Salesky & Anderson (2020) and Laskari, Saxton-Fox & McKeon (2020) all identified the role of coherent structures in wall-normal turbulent transport processes, and Salesky & Anderson (2020) proposed a model to capture their modulating influence in the flux–gradient relationship.

1.3. *Current work*

The current work focuses on building on this existing understanding and further elucidating the role of the turbulent structures in influencing the local transport of a passive scalar. The previous experimental studies that have explicitly looked into the role of coherent structures and high-Re_τ effects involved either point measurements (Talluru *et al.* 2017, 2018, 2019; Talluru & Chauhan 2020) or flow-field measurements performed in water (due to diagnostic simplicity) (Vanderwel & Tavoularis 2014, 2016; Eisma *et al.* 2021). The former provide limited spatial information, while the latter have high-Schmidt-number (Sc) effects at high wavenumbers (Buch & Dahm 1996, 1998). Additionally, the previous measurements predominantly focused on plume structure and mixing in stage 3 where the plume occupies a significant fraction of the boundary layer. We hypothesise that the action of coherent structures in the region immediately downstream of the injection point (stage 2, where the injected plume destabilises into discrete scalar pockets) will have a significant impact and footprint on the downstream evolution into a continuous scalar field. To this end, the current work aims to provide a spatial description of the discrete plume structure, intermittency and arrangement between 1δ and 3δ from the injection point. To facilitate this, we implement quantitative acetone-PLIF (Ac-PLIF) synchronously with PIV in a high-Reynolds-number boundary layer. This technique is similar to that in Connor *et al.* (2018), but for controlled boundary-layer injection within the boundary layer, and measured simultaneously with the velocity flow-field information.

2. Experimental set-up

2.1. *Facility and diagnostics*

The experiments were conducted in a low-speed wind tunnel with a cross-section of 152 mm × 152 mm and a length of 1.42 m. The boundary layer grows on the smooth, bottom surface of the wind tunnel, and is tripped using a cylindrical rod. A small tube with a diameter of $d_i/\delta = 0.026$ (0.625 mm) was used to inject an acetone–air mixture at two heights $h_i/\delta = 0.135$ and $h_i/\delta = 0.307$ which correspond to the boundary-layer logarithmic and wake regions, respectively. We refer to these two injection cases as log-injection and wake-injection cases in this paper. This mixture was injected isokinetically at a velocity of u_{inj} at the two injection points such that $u_{inj} = \overline{U}(y_{inj})$. Measurements were made starting 1.3δ downstream from the injection point, with the field of view spanning $1.4\delta \times 2.0\delta$ in the streamwise–wall-normal plane. The schematic shown in figure 2 illustrates the general experimental set-up.

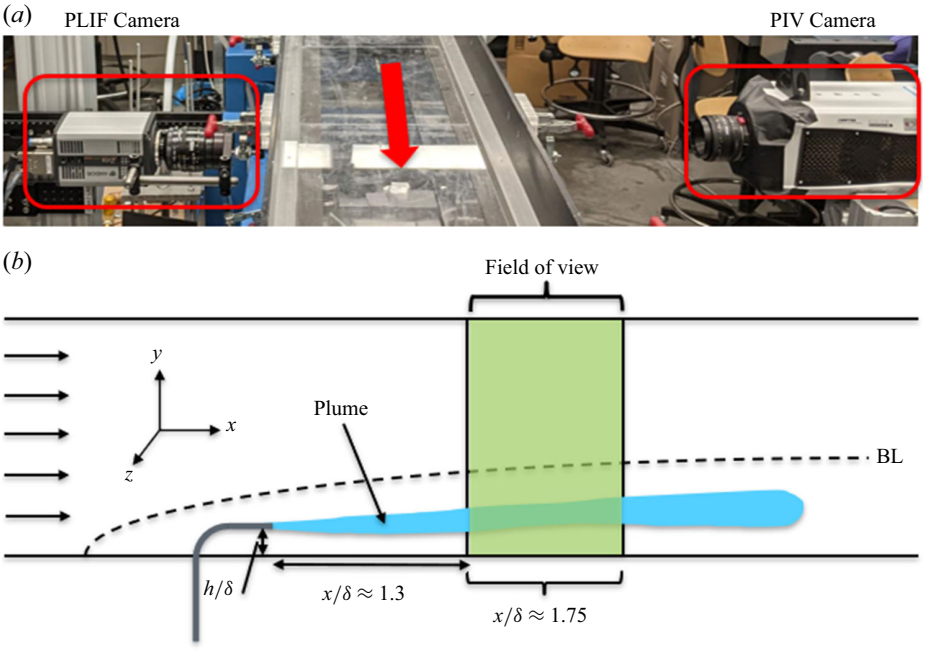

Figure 2. (*a*) Top view of wind tunnel set-up and cameras. (*b*) Schematic side view of experimental set-up. The field of view captures stage 2 evolution from figure 1.

To measure the flow field, simultaneous measurements of scalar and velocity fields were performed using two-component PIV and Ac-PLIF, with synchronised imaging performed from the opposite sides of the laser sheet (figure 2*a*). A single dual-cavity Quantel Q-Smart Nd:YAG laser provided both 532 nm (380 mJ per pulse) and 266 nm (90 mJ per pulse) laser pulses at 10 Hz required for the simultaneous measurements. An extensive optical set-up was necessary to separate and recombine the desired wavelengths from the Nd:YAG laser for optimal performance. Since the raw quadrupled Nd:YAG beam contains 1064 nm + 532 nm + 266 nm, a series of optics were used to isolate the 532 nm + 266 nm wavelengths and dump the 1064 nm into a beam block. The combined 532 nm + 266 nm beams were then focused through a series of spherical lenses and a sheet-forming cylindrical lens. This focused the laser into a thin sheet in the streamwise–wall-normal plane and was projected into the wind tunnel from the optical set-up underneath. Lastly, a BNC Model 575 timing box was used to control the timing of the flash-lamp and Q-switch delay for both laser heads, and the exposure window for both cameras. The PIV camera captured images from both laser pulses while the Ac-PLIF camera captured only the first pulse.

The Mie-scattered light was used to perform planar PIV in the field of view shown in figure 2 using a 4 MP Phantom V641 camera imaging through a 532 nm band-pass filter. A Laskin nozzle filled with olive oil provided the seeding particles necessary for the PIV. The PIV image processing was performed using LaVision Davis 10 with a recursive, multi-pass refinement to a final interrogation window size of $16 \times 16\,\mathrm{px}^2$ with 50 % overlap. Lastly, in post-processing, outlier vectors in the PIV field were filled in using interpolation from the surrounding vectors.

For the injected scalar, an acetone–air mixture was created using an acetone bubbler apparatus consisting of a vertical steel pipe submersed in an acetone bath. Pressurised air entering from the top end of the pipe is forced through small holes at the bottom

end of the pipe submerged in an acetone bath. A heater is wrapped around the acetone bath to increase the temperature and the acetone saturation concentration of the injected plume. The resulting acetone–air mixture created from the bubbler was diverted into two streams. One of the streams was controlled electronically using an MKS-GM50A mass flow controller, and injected into the boundary layer through the injection tube. The excess acetone was vented away. In this way, the injected acetone–air mixture is controlled such that the injected plume is isokinetic with the mean of the incident boundary-layer flow. The Ac-PLIF was performed by exciting the injected acetone gas with the 266 nm laser sheet. The fluoresced light from injected acetone was then imaged with an Andor Zyla sCMOS camera with a 500 nm short-pass filter. The use of this filter greatly reduced the stray fluorescence and reflections from the 266 and 532 nm light by the surrounding materials (mainly the walls/structure of the wind tunnel). The acetone concentration was small enough that absorption of the laser energy across the scalar field is minimal, and we could use an 'optically thin' assumption (Crimaldi 2008). This avoids the need for corrections of Beer–Lambert attenuation. The fields of view of both the PIV and PLIF cameras overlap and both fully capture the laser sheet. To spatially calibrate both fields and overlay them on the same physical space, a symmetric aluminium calibration target visible to both cameras was imaged in the location of the laser sheet. This allowed the PIV and Ac-PLIF data to be projected onto the same plane and simultaneous fields to be calculated. The final calibration and magnification resulted in a vector field resolution of 0.53 mm and a scalar field resolution of 0.078 mm.

2.2. *Corrections to Ac-PLIF*

The raw fluorescence images, I_e (around 2640 uncorrelated, instantaneous snapshots), require several corrections to convert image intensities to quantitative mixture fraction, ξ, measurements. In addition to the fluorescence images of the injected plume, background and laser-sheet profile, I_{cal} images were also taken after each experiment. Background images were taken in the same conditions as those of the actual experiment but with no acetone being injected. This accounts for laser scatter and stray fluorescence/reflections. The laser-sheet profile images were taken by creating a stagnant chamber of acetone vapour of uniform concentration in the wind tunnel, and taking a small ensemble of fluorescence images.

It must be noted that due to the large laser energies involved and the presence of two wavelengths (380 mJ at 532 nm + 90 mJ at 266 nm), the anti-reflective coating and the optics, especially the sheet-forming cylindrical lens, were found to be susceptible to minor damage during the experiment. Due to this, the laser sheet develops striations and local changes in energy as is shown in figure 3(*a*) that translate into noise on turbulent statistics. It was found that this can be compensated to an extent by applying a row-wise parabolic fit to the laser-sheet profile that provides an 'ideal sheet' (figure 3*b*) and accounts for these local imperfections. This was used in lieu of I_{cal} to correct for spatial variations in laser energy.

Finally, after excluding a handful of outlier images (due to laser pulse malfunction), each of the fluorescence images (I) were corrected for background (BG) and laser energy (LS) variations to compute the acetone concentration fields (relative to acetone mole fraction in a calibration experiment), and scaled to injection concentration (I_0) to yield the mixture fraction fields, ξ:

$$\xi = \frac{I - \mathrm{BG}}{\mathrm{LS} - \mathrm{BG}} \times \frac{1}{I_0}. \tag{2.1}$$

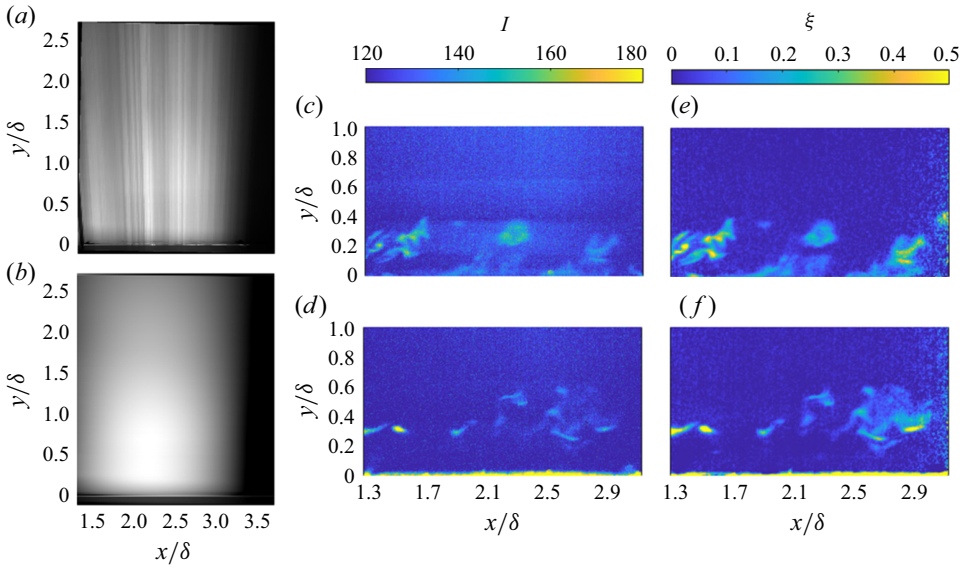

Figure 3. (*a*) Calibration laser intensity image, I_{cal}. (*b*) Ideal laser intensity field, LS. (*c*,*e*) Example fluorescence image (I) and mixture fraction field (ξ), respectively, for the log-injection case. (*d*,*f*) The same for the wake-injection case.

Examples of the LS field, two illustrative initial fields, I, and the corresponding mixture fraction fields, ξ, are shown in figure 3 for log- and wake-injection cases. Median and Gaussian filtering (3 pixels) were used to remove the speckle and high-frequency noise, respectively. The final fields were mapped to world coordinates using LaVision Davis 10 based on the calibration image so that they overlie onto the PIV vector field down to pixel resolution.

2.3. *Boundary layer and injection parameters*

Preliminary PIV data were gathered for three different cases to characterise the incident boundary layer, ensure isokinetic injection of the acetone and capture the effects of the physical presence of the injector on the boundary layer and the presence of acetone on the boundary-layer profile. This was to ensure that the injector pipe and acetone injection would not significantly alter the boundary-layer physics. This was conducted for both log injection and wake injection in three PIV experiments performed in the field of view of interest. (i) First, the unperturbed boundary layer without the injector was measured. This is referred to as the 'baseline case'. Then, (ii) the injector was positioned at respective heights without injecting any acetone and the boundary-layer profiles were measured. This is referred to as the 'no injection' case. Finally, (iii) the injector was positioned at respective heights and acetone was injected under isokinetic conditions (relative to the mean flow). This is referred to as the 'isokinetic injection' case, which is the focus of the the current study.

The mean boundary-layer profiles are shown for all three cases for the log and wake injection in figure 4(*a*,*b*). For both injection locations, the 'no injection' case seems to shift the velocity profile downwards from the wall until around $y^+ = 300$ due to blockage of the injector stem. The 'isokinetic injection' case seems to help the boundary layer recover and more closely resemble the canonical boundary layer compared with the

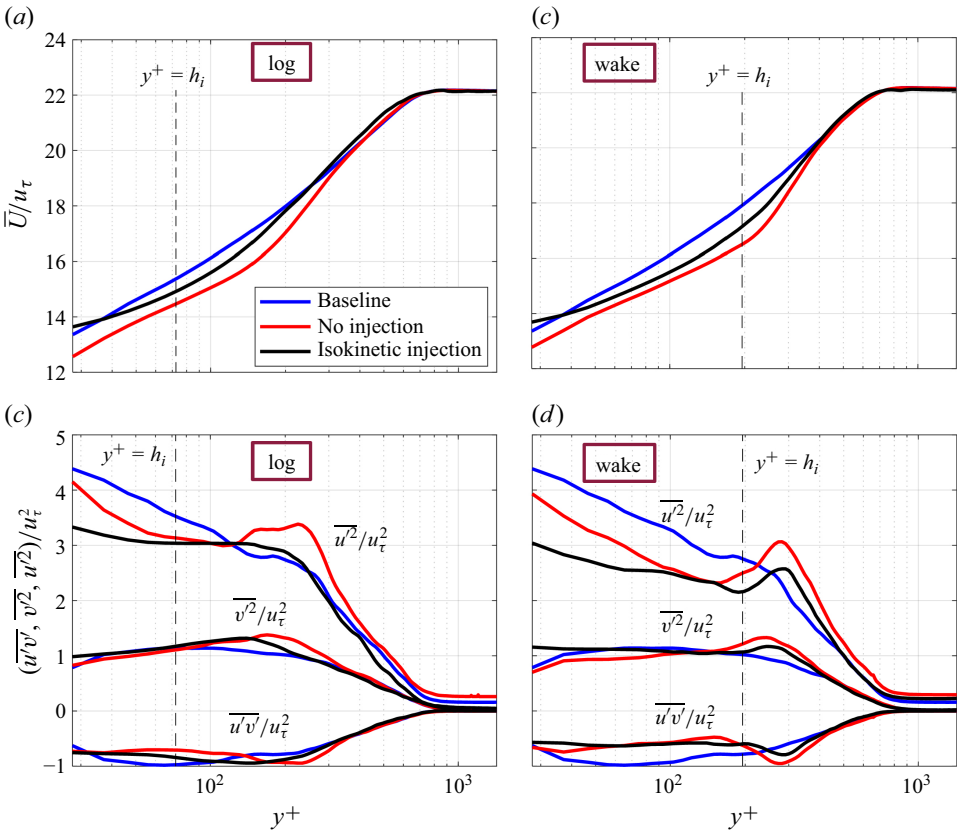

Figure 4. Boundary-layer profiles (*a*,*b*) and Reynolds stresses (*c*,*d*) for both injection locations.

'no injection' case. Except for minor differences, the boundary-layer profiles follow the same trend for baseline and isokinetic injection cases.

We also compare the changes in in-plane Reynolds stresses, as shown in figure 4(*c*,*d*). The injection, no flow case and isokinetic injection case for the streamwise Reynolds stress deviate from the canonical case close to the wall, possibly due to the wake of the vertical injector stem. Away from the wall, the values of all three cases converge on the canonical value for the streamwise stress. Interestingly, there seems to be a jump in all three stresses at a location just before $y^+ = 200$ for both injection locations. This jump is more prominent and noticeable for the wake injection. Nonetheless, for both cases the stresses quickly converge back to a common value consistent with the canonical profile. Overall, the wake injection has more persistent deviation from the canonical case than the log injection, and for both cases the streamwise Reynolds stress has the greatest deviation from the canonical profile. Despite these deviations, the overall trends of the three stresses for canonical and isokinetic injection cases are very similar.

The relevant boundary-layer characteristics for the canonical case are summarised in table 1, and these values are used for all normalisations in the current work. Note that we use δ to refer to δ_{99} defined in table 1 for the reminder of the paper. The boundary-layer inner-scale parameters, namely u_τ, y^* and Re_τ, were estimated by finding the best fit of the measured mean boundary-layer profile to the zero-pressure-gradient composite profile proposed by Chauhan, Monkewitz & Nagib (2009).

Description	Parameter	Value
Injection height	h_i/δ	0.135 (log), 0.307 (wake)
Free-stream velocity	U_∞	10.67 m s^{-1}
Skin-friction *Re*	Re_τ	972
Boundary -layer thickness	δ_{99}	24 mm
Friction velocity	u_τ	0.48 m s^{-1}
Inner length scale	y^*	3.52×10^{-5}
Injector diameter	d_i/δ	0.026

Table 1. Incident boundary-layer characteristics.

2.4. *Simultaneous PIV–PLIF snapshots*

Four representative instantaneous fields are shown in figure 5 that display the overlapped velocity and mixture fraction data for log and wake injection. Gaussian low- and high-pass filters of lengths 1.25δ and $2\times$ vector spacing, respectively, were applied to the velocity field to filter out the large-scale local advection and high-frequency noise (Adrian *et al.* 2000*a*). This demonstrates the ability to perform simultaneous field measurements of quantitative scalar mixture fraction and turbulent velocity flow fields and qualitatively highlights the turbulent dynamics responsible for scalar transport within the boundary layer. We utilise this capability to capture the spatial organisation of the scalar dispersion relative to the coherent motions of the boundary layer akin to those obtained by point measurements by Talluru *et al.* (2018) and Talluru & Chauhan (2020), and calculate scalar two-point auto- and cross-correlations using simultaneous spatial measurements.

3. Mean plume evolution and analytical models

The mean values of u, v and ξ in the plume were calculated by taking the ensemble average of the roughly 2600 fields after the corrections have been applied as described in § 2. These mean values were then used to calculate the perturbation fields of u, v and ξ and turbulent fluxes in each field.

The evolution of the mean concentration profile as a function of downstream location follows a reflected Gaussian function of form (3.1) first proposed by Fackrell & Robins (1982*b*). Figures 6 and 7 show the mean and variance plots for the log and wake injection, respectively, with a line plots of the contour shown at three streamwise locations. For the mean concentration line profiles, (3.1) is also shown fitted to the mean concentration data at the chosen downstream locations showing an excellent fit for both injection locations. The variance plots for both log and wake injection both seem to follow a rough reflected Gaussian distribution with a peak at the injection height, as was previously observed by Fackrell & Robins (1982*b*) and Miller (2005).

Many previous studies have utilised single-point measurements to understand plume dispersion in TBLs. Nironi *et al.* (2015) compared experimentally measured plume dispersion with analytical models based on hypotheses from Fackrell & Robins (1982*a*,*b*) with good agreement, the procedure for which is followed here. This equation assumes the interaction of the plume with the wall and accounts for this via a virtual source below the wall at a wall-normal location of $y = -h_i$, given as

$$\overline{c}(x, y) = \frac{M_q}{2\pi\sigma_y\sigma_z\overline{u}_{adv}}\left[\exp\left(-\frac{(y+h_i)^2}{2\sigma_y^2}\right) + \exp\left(-\frac{(y-h_i)^2}{2\sigma_y^2}\right)\right], \tag{3.1}$$

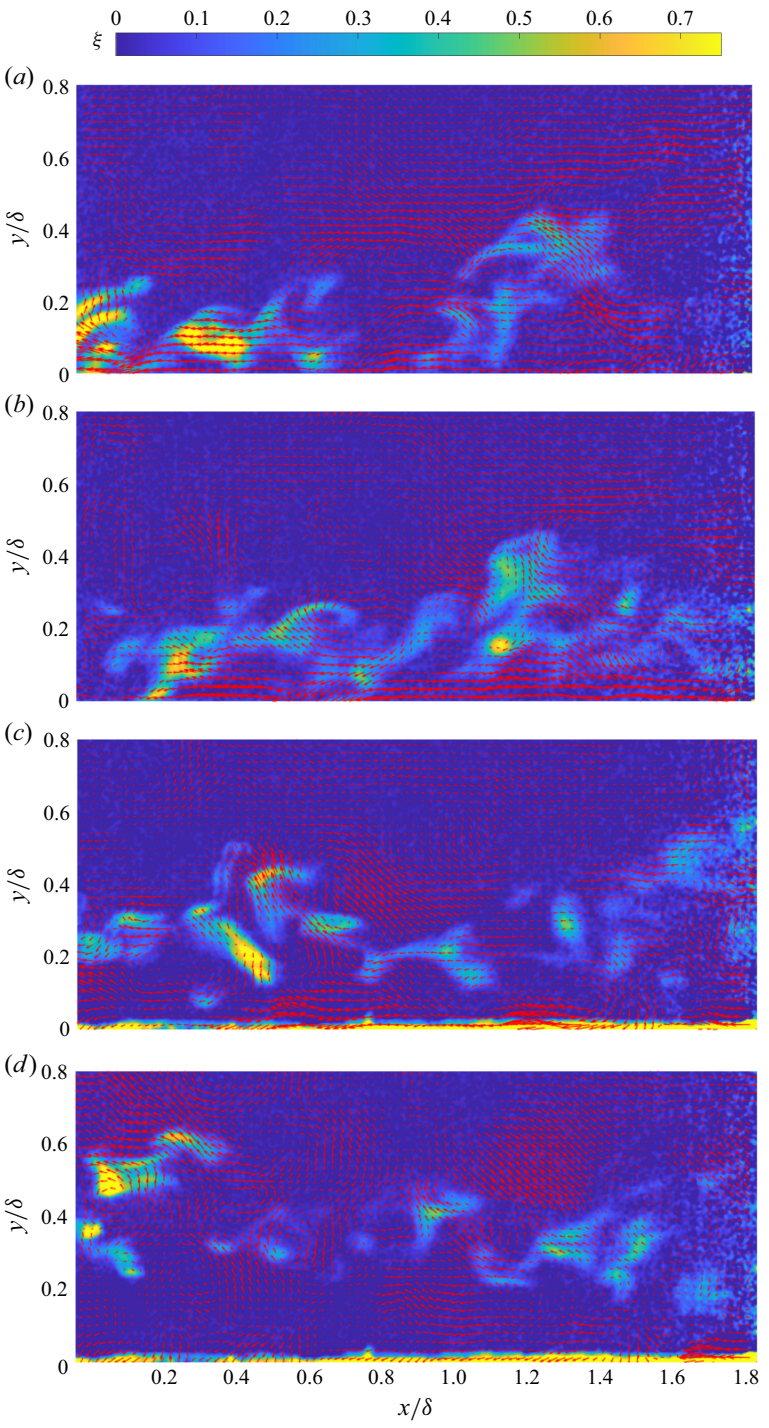

Figure 5. Instantaneous snapshots of simultaneous mixture fraction ($\tilde{\xi}$) and band-pass-filtered velocity fields for (*a*,*b*) log-injection and (*c*,*d*) wake-injection cases.

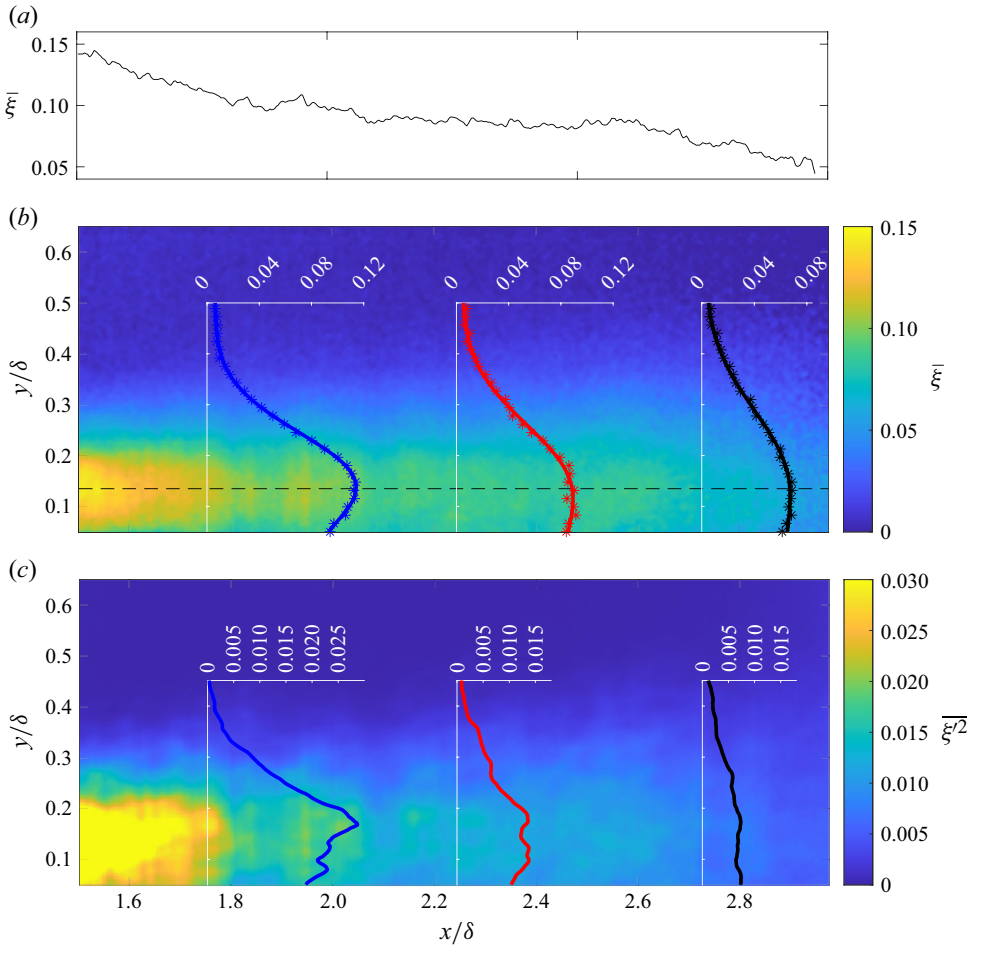

Figure 6. Log-injection case: (*a*) mean mixture fraction on injection line $\overline{\xi}(y = h_i)$, (*b*) mean mixture fraction $\overline{\xi}$ field and (*c*) variance of mixture fraction field $\overline{\xi'^2}$.

with M_q denoting the mass flux from the injector, σ_y and σ_z denoting the plume spread in the wall-normal and spanwise directions, respectively, and h_s denoting the injection height of the plume. By using the best fits to the mean profile (figures 6 and 7), the various parameters can be extracted. However, since only the wall-normal plume spread σ_y is available from the PLIF measurements, the spanwise plume spread, σ_z, is approximated as $\sigma_z \approx \sigma_y$. This assumption is necessary to calculate all the variables in (3.1). This approximation holds reasonably well for elevated sources as was illustrated by Nironi *et al.* (2015, figure 6) (though the wall-normal plume is typically slightly less than the spanwise spread).

This wall-normal plume spread, σ_y, can also be estimated analytically via the Lagrangian transport and dispersion of the scalar plume. A Lagrangian plume, growing in time t in a turbulent environment can be described as (see Fackrell & Robins 1982*b*)

$$\sigma_y^2 = \frac{\sigma_0^2}{6} + 2\sigma_v^2 T_{Lv}\left(t - T_{Lv}\left[1 - \exp\left(-\frac{t}{T_{Lv}}\right)\right]\right), \tag{3.2}$$

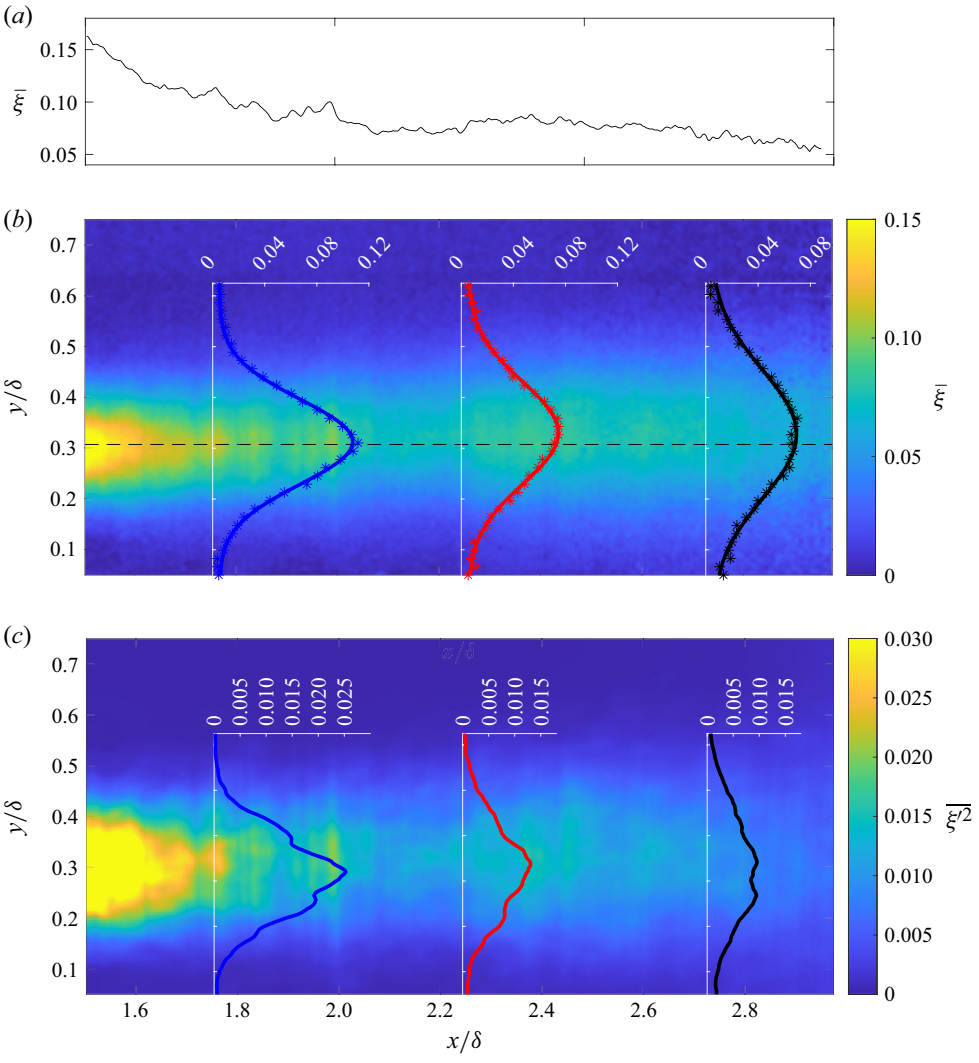

Figure 7. Wake-injection case: (*a*) mean mixture fraction on injection line $\overline{\xi}(y = h_i)$, (*b*) mean mixture fraction $\overline{\xi}$ field and (*c*) variance of mixture fraction field $\overline{\xi'^2}$.

with σ_0 being the equivalent initial plume diameter (typically $= d_i$), σ_v^2 the variance of the turbulent velocity fluctuation and T_{Lv} the Lagrangian time scale of the turbulent environment. The time in (3.2) can be converted to spatial distance using Taylor's frozen field hypothesis (i.e. $t = x/U$). Assuming isotropy in turbulence, the Lagrangian time scale T_{Lv} can be approximated by the Eulerian integral length scale L_{vv} using (3.3):

$$T_{Lv} = \frac{L_{vv}}{\sigma_v^2} = \frac{L_{vv}}{\overline{v'^2}}, \tag{3.3}$$

with $\overline{v'^2}$ denoting variance of velocity perturbation in the wall-normal direction. Finally, the integral transverse length scale, L_{vv}, can be estimated by fitting an exponential decay to the auto-correlation of v' in the wall-normal direction. More details can be found in Nironi *et al.* (2015).

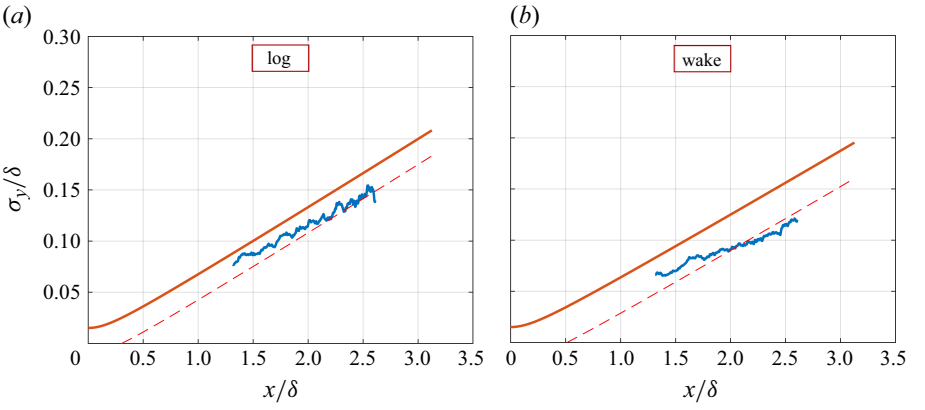

Figure 8. Comparison of theoretical plume spread (red) predicted by (3.2), experimental plume spread (blue) obtained by fitting (3.1) to the current data and theoretical plume spread offset vertically for reference (dashed line).

Since the turbulent velocity fields were measured, the properties of (3.2) can be calculated to form the theoretical plume spread, and compared against the σ_y measured experimentally. This comparison is shown in figure 8 for both log- and wake-injection cases. It can be seen that the overall trends of the plume spread are accurately captured by the model, with some discrepancies. The plume in the current experiments appears to be offset from that predicted by the model for the logarithmic region. This can be associated with the weak definition of σ_0, which is an effective source plume width not always exactly equal to the source diameter, d_i. For the wake region, the plume is offset and appears to grower slower than that predicted by the model. The authors suspect this to be from the large size of the injector relative to the boundary layer (d_i/δ) and the limitations of indirectly estimating the Lagrangian time scales using (3.3) in the intermittent wake region. It should also be noted that the non-dimensionalised injection diameter of the current experiment is an order of magnitude larger than that seen in Nironi *et al.* (2015), which can add finite source-diameter effects not captured by the models. This can possibly be corrected via a virtual origin consideration, though is not the focus of the current work.

4. Turbulent scalar fluxes

The simultaneous measurement of scalar and turbulent velocity fields enables us to compute the turbulent scalar fluxes in the measurement plane (i.e. $\overline{u'\xi'}$ and $\overline{v'\xi'}$). Since the scalar fields are acquired at higher spatial resolution than the velocity fields ($(0.078\ \mathrm{mm})^2$ versus $(0.530\ \mathrm{mm})^2$), the scalar fields are downsampled to the velocity field resolution to estimate these cross-statistics. Contour and line plots of $\overline{u'\xi'}/u_\tau$ and $\overline{v'\xi'}/u_\tau$ are shown for the log- and wake-region injection points in figure 9. The contour plots show clear trends in both regions centred around the injection point. For the streamwise perturbations (u') there are on average positive correlations with ξ' below the injection line and negative correlations above the injection line. The wall-normal flux shows a positive correlation above the injection point and a negative correlation below, mirroring the trend seen for the streamwise flux. There is also a distinct net zero flux region at the injection line for the wall-normal flux, and just below the injection point for the streamwise flux. This will asymptote to the injection height further downstream as plume transport loses memory of the injector and it evolves towards stage 3 mixing. These trends are consistent with

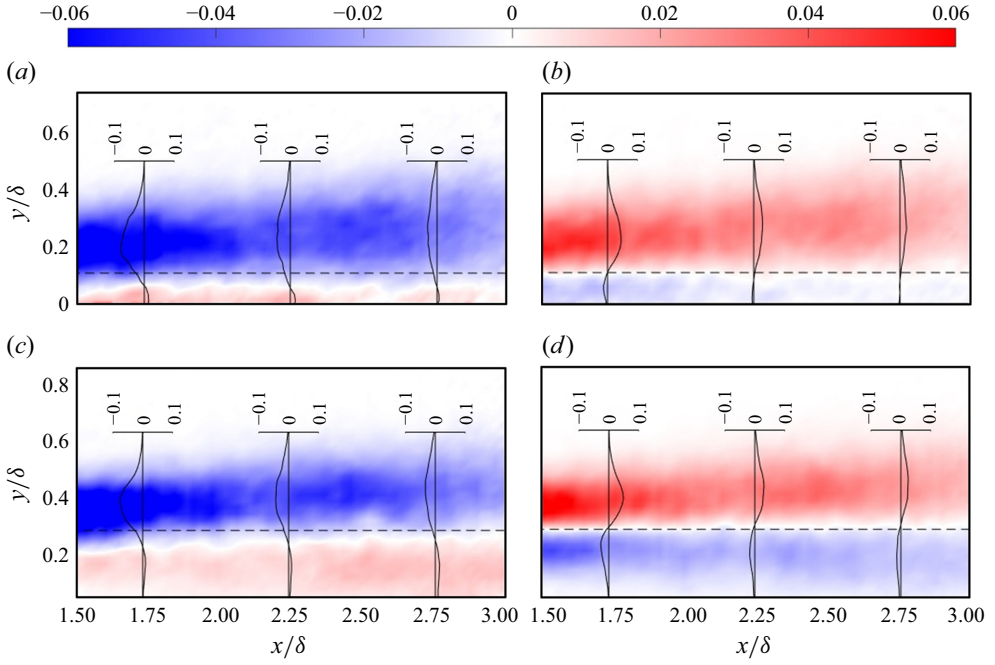

Figure 9. (*a*,*c*) Streamwise ($\overline{u'\xi'}/u_\tau$) and (*b*,*d*) wall-normal ($\overline{v'\xi'}/u_\tau$) turbulence scalar flux for (*a*,*b*) log-injection and (*c*,*d*) wake-injection cases.

the existing literature (e.g. Fackrell & Robins 1982*a*; Crimaldi *et al.* 2002; Nironi *et al.* 2015; Talluru *et al.* 2018), and for a mean plume spreading in wall-normal and spanwise extents. The mean transport of a high-concentration pocket of fluid ($\xi' > 0$) originally at the injection line away ($v' > 0$) and towards ($v' < 0$) the wall will have positive and negative values, respectively, of wall-normal turbulent flux, $\overline{v'\xi'}$. Similarly, the streamwise turbulent flux, $\overline{u'\xi'}$, away from the injector line will have the opposite sign to $\overline{v'\xi'}$ owing to the mean negative Reynolds shear stress in the entire boundary layer, i.e. $\overline{u'v'} < 0$.

4.1. *Two-point mixture fraction correlation*

The spatial scalar fields enable us to compute the multi-point turbulent statistics directly, without the need for Taylor's hypothesis. The two-point mixture fraction correlation, $R_{\xi\xi}$, defined by (4.1), is computed to understand the spatial coherence of the scalar:

$$R_{\xi\xi}(\Delta x, \Delta y; x_r, y_r) = \frac{\langle \xi'(x_r, y_r)\xi'(x_r + \Delta x, y_r + \Delta y)\rangle}{\langle (\xi'(x_r, y_r))^2\rangle}. \tag{4.1}$$

These correlations represent the general shape, extent and inclination of the mixture fraction neighbourhood around (x_r, y_r) (where a certain value of mixture fraction, ξ', is detected). Previous studies (Miller 2005; Talluru & Chauhan 2020) using point measurements (and Taylor's hypothesis) have shown that the two-point mixture fraction correlation fields are inclined at an angle to the horizontal, where the location of maximum correlation above the reference location ($y > y_r$) is ahead in streamwise location ($x > x_r$), and vice versa. To investigate this phenomenon spatially using the current data, the correlation fields were calculated using (4.1) for $y_r = h_i$ at various streamwise locations, x_r. Further, to achieve reasonable convergence, these fields were locally averaged over streamwise spans of 0.65δ and 0.7δ for the log and wake injection, respectively (assuming

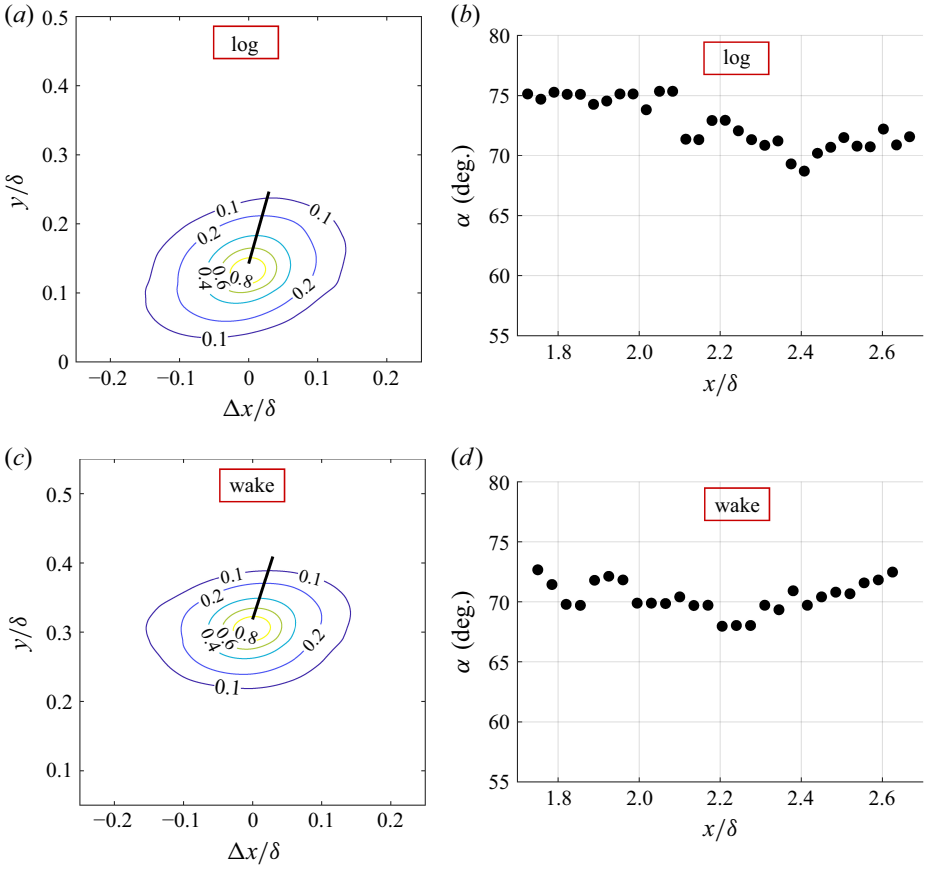

Figure 10. Angle of maximum mixture fraction correlation for (*a*,*b*) log injection and (*c*,*d*) wake injection. (*a*,*c*) Illustrative local correlation maps at $x/\delta = 1.9$ for the two cases.

local homogeneity over those distances). To find the inclination angle, α, the maximum $R_{\xi\xi}$ was found for each wall-normal location and a line was fitted to these points. This process is illustrated in figure 10(*a*,*c*). The angle between this line and the horizontal is the angle of inclination, similar in approach to that of Talluru & Chauhan (2020) (who did this using temporal, point measurements).

Figure 10(*b*,*d*) shows the variation in the inclination angle, α, with increasing downstream distance for log- and wake-injection cases. The inclination angle for the log-region injection decreases downstream showing a change of roughly 5° in inclination angle across the measurement domain. This is likely due to the strong straining and rotation that the scalar plume experiences early on as it is transported away from the wall due to the turbulent mechanisms. Figure 10(*d*) shows that, for wake injection, the inclination angle is roughly constant. This can be associated with the smaller shear experienced by the plume when dispersed within the wake region.

Talluru & Chauhan (2020) calculated and discussed this inclination angle using temporal measurements with two synchronised point sensors. From their measurements, they observed an inclination angle ranging from 29° to 31° depending on the injection height. Similar two-point scalar correlations using scalar field measurements were also performed by Miller (2005) for various downstream distances. They observed that the correlation contours start isotropic close to the injection location (i.e. $\alpha \approx 90°$) and then

increasingly incline with downstream distance (i.e. decreasing α). These trends are similar to those observed in the current work. The exact streamwise variation of this angle close to a point source (i.e. stage 1 and stage 2 mixing) and the dependence on the boundary layer and injection/injector parameters are not studied in sufficient detail. It appears that these scalar concentrations approach the inclination angles comparable to that of R_{uu} at very large distances from the injector (Tavoularis & Corrsin 1981; stage 3). Close to the injector, we suspect that this angle is a strong function of the advection velocity, distance and the mean vorticity experienced by the plume. From this standpoint, the relative size of the plume compared with the boundary-layer thickness (σ_y/δ) becomes relevant, which is directly proportional to the injector diameter. This is significantly different between the current work ($d_i/\delta = 0.026$) and Talluru & Chauhan (2020) ($d_i/\delta \approx 0.005$) which likely accounts for the differences between the two works. However, it is still unclear how the plume parameters (x/δ, y/δ, σ_y/δ etc.) influence this inclination angle and further studies are necessary to understand these relationships.

5. Scalar intermittency and 'blob'-like behaviour

The turbulent mixing of the plume can be described phenomenologically in three stages as seen in figure 1. The first stage lasts for a relatively short distance where the plume forms a laminar stream in the boundary layer. The shear forces and turbulence within the boundary layer destabilise the plume which quickly transitions into the intermediate stage (stage 2). This stage of mixing is characterised by discrete parcels of concentrated fluid, hereafter referred to as 'blobs' due to their appearance in the plane of measurement (note that these streaks extend continuously out of the plane). After the blobs have formed, they may break up into smaller blobs, be strained into elongated streaks or diffuse and mix as small-scale turbulent motions ($\mathcal{O}(< D_p)$, where D_p is the local plume diameter). As this process continues over large downstream distances, the scalar field expands throughout the boundary layer, becomes less intermittent and forms a continuous scalar field (stage 3).

The entirety of the plume evolution (stages 1–3 in figure 1) has been investigated with experimental and theoretical endeavours. However, the intermediate or transitional stage has been difficult to characterise and lacks the breadth of investigation afforded to the initial and late stages of plume evolution. The current study focuses on this intermediate stage and attempts to characterise it by describing the statistical characteristics of blobs captured in the instantaneous fields. To this end, roughly 2670 mixture fraction fields were captured for each injection location and the data were extracted from the blobs in each frame. Figure 11 details this process for an example mixture fraction field (figure 11*a*). This image is thresholded to create a mask (figure 11*b*) using a threshold of $\xi_{th} = 0.225$. The choice of this threshold was guided with the goal of detecting large regions of high-concentration blobs of marked scalar. We intentionally excluded (i) small regions of high concentration (mostly from speckle noise) and (ii) large regions of diffused/well-mixed marked scalar. Threshold ξ_{th} was defined quantitatively to be the 90th percentile of the distribution of ξ values above the noise floor. Applying this threshold provides the discrete boundaries of the blobs of high concentration, and the closed regions are then catalogued. Finally, an area filter is applied where any blob with an area less than a minimal threshold, $A_{th} = 15\ px^2 = 1.58 \times 10^{-4}\ \delta^2$, is disregarded, effectively serving as a noise filter to exclude random bright spots. For each blob, the area ($\tilde{A}$), average mixture fraction ($\tilde{\xi}$), aspect ratio ($\widetilde{AR}$), inclination angle with respect to the wall ($\tilde{\phi}$) and centre of mass ($\tilde{x}_{cm}$, $\tilde{y}_{cm}$, marked in figure 11*c*) were extracted (note that we use a tilde to represent blob properties). A total of 75 866 blobs were captured for both injection locations, which was reduced to 42 019 blobs after the area thresholding.

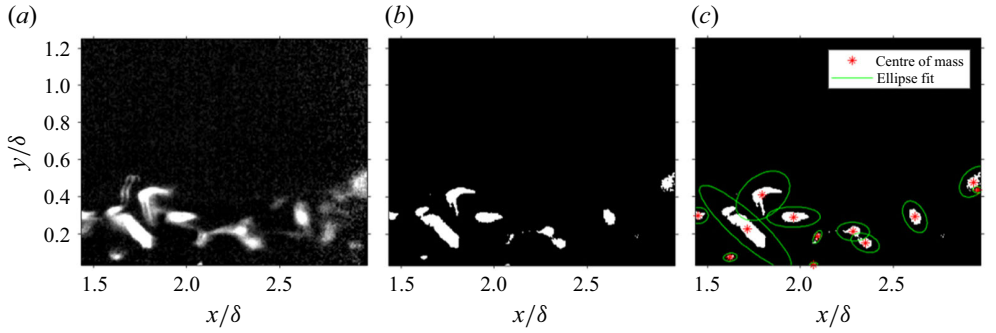

Figure 11. Example of processing to identify and extract blob properties: (*a*) corrected image, (*b*) mask applied and (*c*) area filter applied and centre of mass location identified.

Using this catalogue of blobs, we first study the concentration and coordinate data of the blobs to validate the meandering plume model proposed by Gifford (1959) and Fackrell & Robins (1982*a*,*b*) and expanded on by Talluru & Chauhan (2020). Secondly, the relationship between blob area $\tilde{A}$ and density $\tilde{\rho} = \tilde{\xi}/\tilde{A}$ is investigated through the joint PDFs. The proposed relationship between area and density provides insight into blob dynamics in the intermediate region. Finally, the inclination angle and aspect ratio are investigated to provide insight into the physical shape and orientation of the blobs.

5.1. *Scaled probability of concentration at different injection points*

Gifford (1959) presented the meandering plume model (also discussed in Marro *et al.* (2015)) in which the plume mixing occurs through two simultaneous phenomena captured via their PDFs. The first component of this model is the meandering of the centre of mass (p_m in (5.1)) of the plume where large-scale structures transport the entire plume along the wall-normal and spanwise directions. The second component of the theory encompasses the local dissipation of the plume through small-scale turbulence and random molecular motion (p_{cr} in (5.1)):

$$p(\xi; x, y, z) = \int_0^\infty \int_{-\infty}^\infty p_{cr}(\xi, x, y, z; y_m, z_m)\, p_m(y_m, z_m; x)\, \mathrm{d}y_m\, \mathrm{d}z_m, \tag{5.1}$$

with ξ denoting the mixture fraction, x, y, z denoting the streamwise, wall-normal and spanwise positions, respectively, and y_m and z_m denoting the y and z locations of the centre of mass. Critically, the model assumes that the two processes are independent of each other, an approximation that holds in high-*Re* boundary layers when the plume diameter $D_p \ll \delta$ (i.e. $p_{cr} = fn(\xi, x, y - y_m, z - z_m$ only)). This implies that, in the frame of reference of the plume's centre of mass, its statistical characteristics (such as distributions of concentration, inclination angle, aspect ratio etc.) for a given x will be independent of y and z. In other words, if the plume meanders to a given location, then its statistical characteristics should be identical to those of other wall-normal locations (though the probability of this meandering, p_m, will be different).

We evaluate this condition via the PDF of the average mixture fraction, $\tilde{\xi}$, for both the log- and wake-injection cases. Figure 12 shows the scaled (by maximum value) blob concentration probabilities at different wall-normal distances from the injection point. The data suggest that while the average total concentration decreases further from the injection point, the distribution of blob concentration at an arbitrary distance from the injection point seems to be identical. Phenomenologically this suggests that blobs of

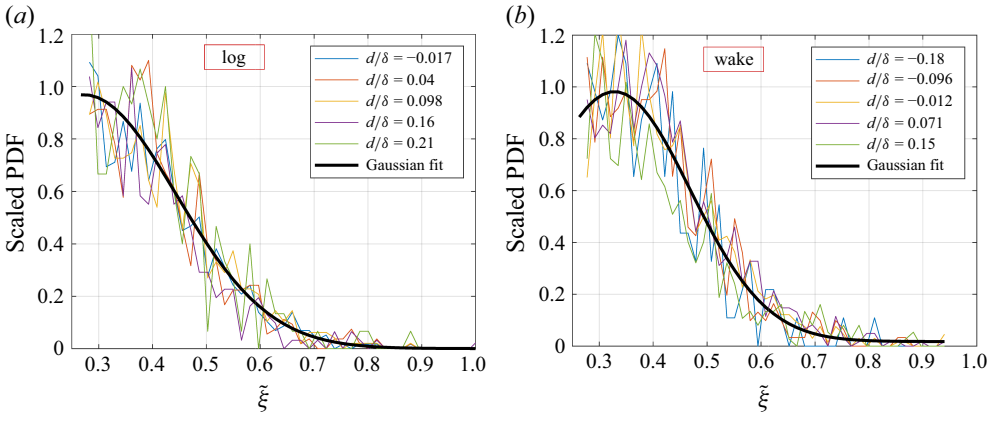

Figure 12. Normalised PDF of $\tilde{\xi}$ at different wall-normal distances from the injection location for (*a*) log-injection and (*b*) wake-injection cases.

different concentrations indiscriminately meander from the injection line such that the statistical distributions of the concentration of the blobs at any wall-normal distance form the injection line are identical. This supports the statistical independence of the meandering and dispersion mechanisms described in the meandering plume model. However, further studies, ideally with a well-converged dataset and a range of injection locations, are necessary to confidently establish the statistical independence between wall-normal location and distribution of blob mixture fraction.

5.2. *Relationship between blob density and area*

Using the blob database, we try to understand the mechanisms by which the discrete blobs 'break up' and 'disperse' into a continuous field, as was shown in figure 1. Both these processes change the area of the scalar blobs observed. An ideal 'breakup' occurs due to locally diverging vector topology (saddle-like topologies in plane), and preserves the average concentration of scalar in the blob (i.e. $\tilde{\xi}$). The 'dispersion' occurs due to micromixing by small-scale local turbulence ($l \ll D_p$), and preserves the amount of substance in the blob (i.e. $\tilde{\xi}\tilde{A}$). Even though the transport is a three-dimensional phenomenon, these two processes can be statistically visualised using the distribution of blob areas and concentrations in the symmetry plane.

Figure 13 shows the joint PDF of scalar density (defined as $\tilde{\rho} = \tilde{\xi}/\tilde{A}$) and blob areas ($\tilde{A}$) for the log- and wake-injection cases. Both cases show a distribution of $\tilde{\rho}$ and $\tilde{A}$. For a pure breakup event, where a blob breaks up into smaller blobs, the area would decrease but the average mixture fraction $\tilde{\xi}$ would be conserved. A successive progression of this process will result in a distribution of blobs cascading up a curve of $\tilde{\rho} = k_1/\tilde{A}$ (k_1 is an arbitrary constant depending on the initial concentration). The solid red line represents an example of this with $k_1 = 0.3$ ($k_1 = 0.25$ provides the best fit assuming only blob breakup). On the other hand, should the blob change in physical size due to diffusion, the area changes to conserve the material, $\tilde{m} = \tilde{\rho}\tilde{A}^2$. This results in a cascade along the line $\tilde{\rho} = k_2/\tilde{A}^2$ (k_2 is a constant depending on initial blob mass). The dashed lines in figure 13 represent this diffusion cascade for several k_2 values illustrating how dispersion causes the blob evolution to stray from the purely breakup case (solid line). Given an initial distribution of blobs with large area and low $\tilde{\rho}$ (bottom right of figure 13),

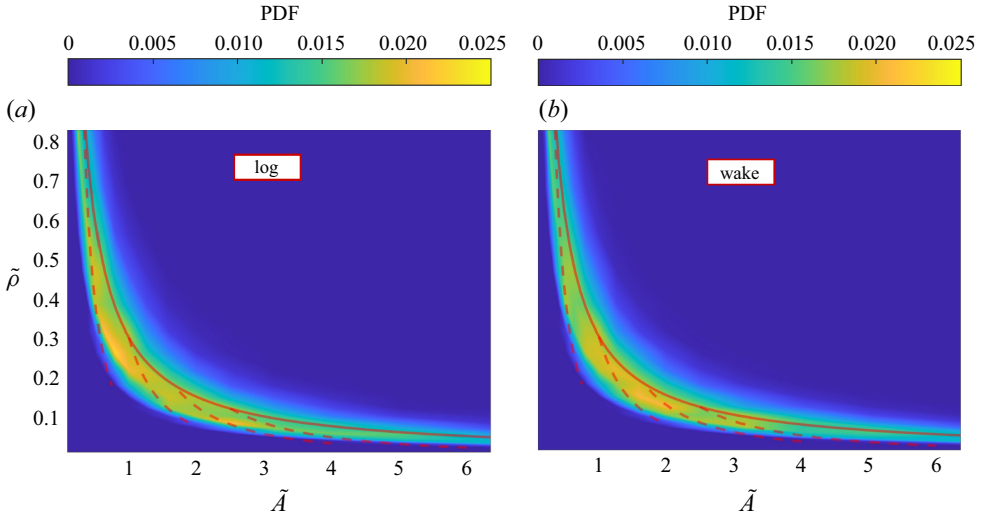

Figure 13. Joint PDF of $\tilde{\rho}$ and area $\tilde{A}$ for (*a*) log-injection and (*b*) wake-injection cases.

the evolution of these blobs along a purely breakup trajectory would account for the general shape of the joint PDF including some of the spread perpendicular to the $\tilde{\rho} = k/\tilde{A}$ line. The spread of the joint PDF perpendicular to this line of $\tilde{\rho} = 0.25/\tilde{A}$ arises from both the variation in initial blob size and the dispersion along the dashed lines (diffusion). The strong trends of the joint PDF along the breakup line, and weak spread perpendicular to it, indicate that blob breakup is the primary mechanism of plume evolution in the streamwise extent considered. However, as the plume disperses within the boundary layer further downstream and the scalar spectrum develops length scales $\mathcal{O}(\delta)$, dispersion is expected to play a more significant role, limiting the utility of this discrete blob approach.

The evolution of the blob area and mean concentration as a function of streamwise location can also be investigated to determine the dominant mechanism of plume evolution. If the plume evolution at this stage is breakup-dominated, then the average area should decrease as the streamwise position increases. Since breakup does not change the mixture fraction $\tilde{\xi}$, it should stay relatively constant. Alternatively, if the plume evolution is dispersion-dominated, the opposite trends are expected. The average area of the blobs should increase with streamwise position, with an associated decrease in the mean mixture fraction. The trends of blob mixture fraction and area as a function of streamwise location can be seen in figure 14. The evolution of the average blob area ($\overline{\tilde{A}}$) shows a marked decrease across the field of view. The intermittent peaks in the average blob area (figure 14*b*,*d*) are likely caused by the lack of convergence. The average mixture fraction of the blobs ($\overline{\tilde{\xi}}$) stays relatively constant ($\approx \pm 3\,\%$) across the field of view. The marked decrease in area with downstream location seen in figure 14(*b*,*d*) and the constant value of mixture fraction across the streamwise locations (figure 14*a*,*c*) support the breakup-dominated plume evolution previously discussed.

5.3. *Aspect ratio and inclination angle of blobs*

Besides the size and mixture fraction, the scalar blobs are also elongated and inclined to the horizontal at a certain angle. These characteristics were also investigated using the ensemble. For each blob, an ellipse was fitted to the outline (figure 11*b*) with an

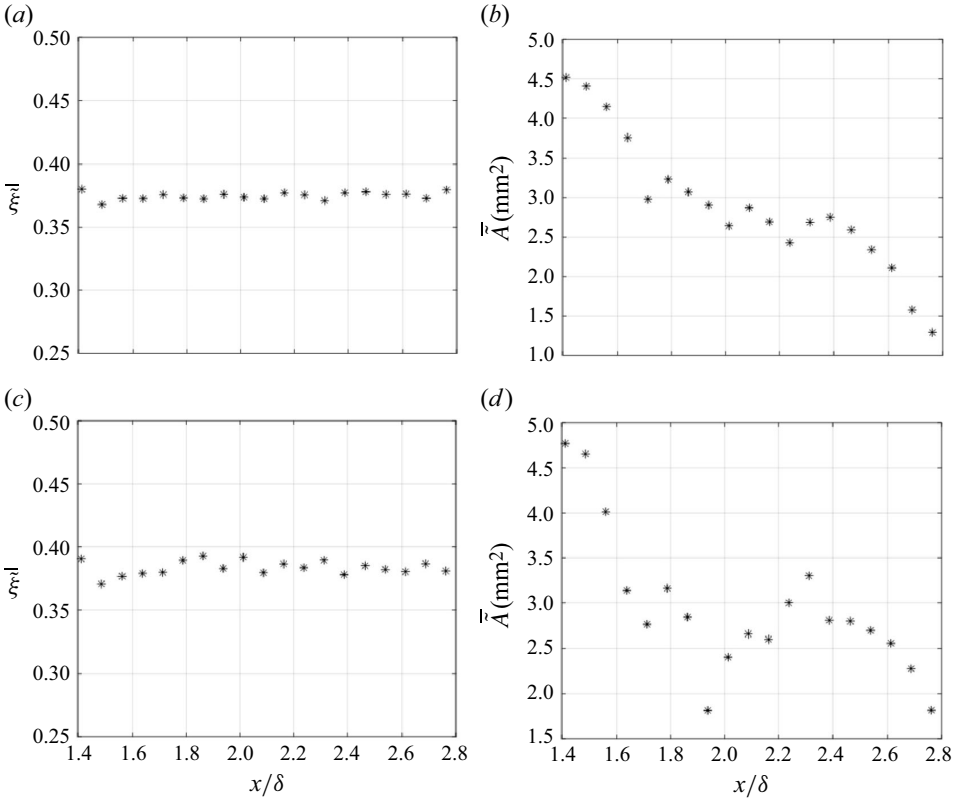

Figure 14. Mixture fraction of the blobs (*a*,*c*) and area of the blobs (*b*,*d*) at different streamwise locations for log (*a*,*b*) and wake (*c*,*d*) injection.

equivalent area moment of inertia about the major and minor axes (MATLAB 2023). The $\widetilde{AR}$ can then be calculated as the ratio of the major to minor axes (a/b), and ϕ as the counterclockwise angle between the horizontal and the major axis of the fitted ellipse. Its important to note that the blobs rarely formed perfect ellipses; however, using this approach provides a consistent method to calculate these two quantities which provide insight into the statistical nature of the blobs' evolution. Inclination angle provides insight into how the blobs tend to rotate and how they are formed, while $\widetilde{AR}$ gives insight into how the blobs tend to be stretched and elongated. Clear trends can be seen in figure 15 for $\widetilde{AR}$ and inclination angle $\tilde{\rho}$ at both injection locations. A normal distribution was fitted to the inclination angle, which provides a good fit to the data. A skewed normal distribution was used to fit the aspect ratio providing a good estimate of the observed measurements.

The constants in table 2 summarise the various constants for the distribution (mean μ and variance σ). It can be seen that there is a clear positive preference for the inclination angle of the blobs in both injection regions. The log injection has a slightly larger inclination angle at 12.5° compared with 10° in the wake injection. This is due to larger shear that the blobs experience as they evolve from the injection height. The standard deviations for both regions are statistically identical. For the aspect ratio, both regions have a peak around 1.6–1.7 with a steep decline in PDF afterwards. Both regions show a strong preference for an elongated ($AR > 1$) shape, with the majority of the blobs having an aspect ratio $1 < AR < 3$. The only notable difference between the aspect ratio distribution for the log and wake injection is the wake distribution in aspect ratio is flatter than in the

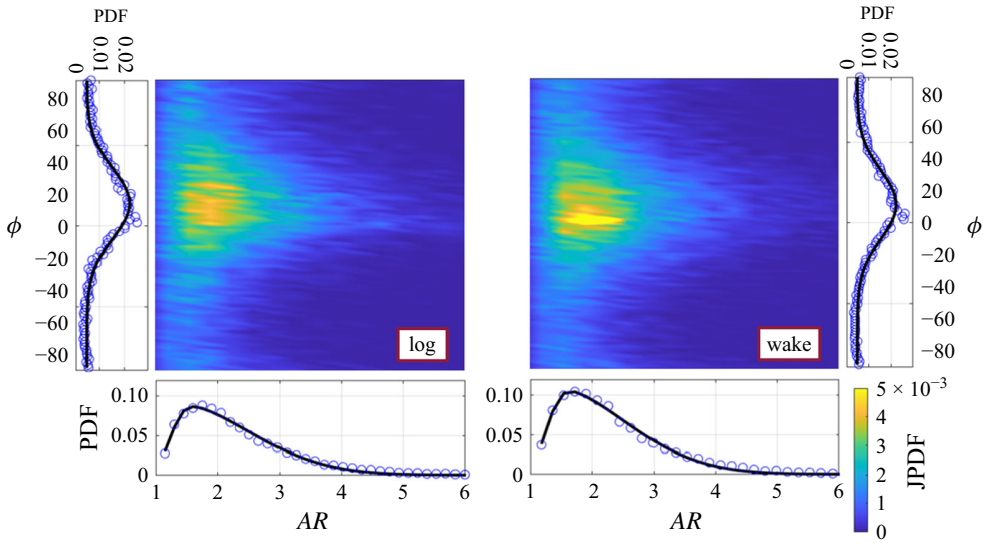

Figure 15. Joint PDFs and PDFs of aspect ratio ($\widetilde{AR}$) and inclination angle ($\tilde{\phi}$) for log- and wake-injection cases.

	Inclination angle ($\tilde{\phi}$)		Aspect ratio ($\widetilde{AR}$)	
—	μ	σ	μ	σ
Log	12.5	21.3	1.17	1.22
Wake	10.1	21.4	1.18	1.18

Table 2. Best-fit distribution constants for the log-injection (left) and wake-injection (right) cases.

log region, likely due to higher mean shear experienced by the log-injected plume and leading to a larger variation in aspect ratios.

6. Spatial coherence in plume intermittency

6.1. *Instantaneous observations*

With the previous observations indicating that the scalar plume is highly intermittent and dispersed into discrete blobs, we can focus on the role of specific turbulence structures in developing the spatial trends. In other words, a continuous injection of the passive scalar is reorganised into intermittent and concentrated pockets by the action of turbulent structures of similar scale. Figure 16 shows instantaneous snapshots of this organisation, in an arbitrary frame of reference moving with the fluid for the two injection configurations. Also shown are the contours of swirling strength, λ_{ci}, that represent the local rotational motion of the fluid elements due to strong vortices (the swirling motion is not immediately evident in the vector field due to advection). The swirling strength λ_{ci} is defined as the imaginary part of the complex eigenvalue of the velocity gradient tensor, and local maxima in its value indicate the location of a vortex element (Chakraborty, Balachandar & Adrian 2005). The current experiments are only capable of capturing the vortex elements sliced perpendicularly by the measurement plane, and the sign of the vorticity is assigned

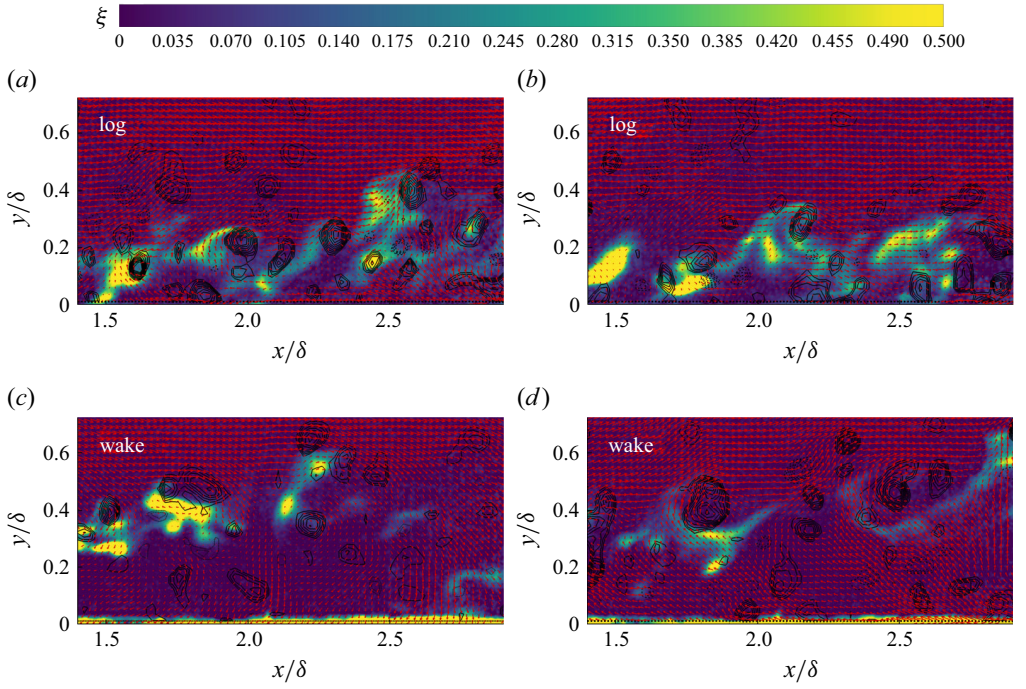

Figure 16. (*a–d*) Instantaneous snapshots showing scalar plume together with contours of swirling strength. Vectors are shown in a frame moving at $\approx 0.88U_\infty$.

to identify the 'prograde' ($\lambda_{ci} \leqslant 0$, clockwise) and 'retrograde' ($\lambda_{ci} > 0$, anticlockwise) vortices (Adrian *et al.* 2000*a*).

A qualitative organisation of the scalar plume relative to the vortex cores is observed in figure 16(*a*,*b*) – a trend that occurs around 25 % of the vector fields. This trend is particularly dominant if the fields are conditioned on a scalar blob occurring far away from the injection location ($y - y_i > 2\sigma_y$). It can be seen that a discrete scalar blob occurs preferentially between the vortex cores, and at an angle inclined $\approx 15° - 18°$. Additionally, multiple vortex cores are observed to be aligned along this line with the distinct signature of the coherent vortex packet (Adrian *et al.* 2000*b*; Christensen & Adrian 2001; Adrian 2007). This alternating inclined scalar-blob–vortex-core organisation was less prevalent when the injection was in the wake region, as illustrated in figure 16(*c*,*d*). The scalar plume was still dispersed and intermittent, and the discrete scalar blobs were mostly attached to a dominant vortex core. However, coherent interlacing of scalar blobs with an inclined set of coherent vortices extending all the way to the wall was not observed for wake injection. This indicates that the action of the vortices (possibly from the detached packets) on the scalar plume is still the dominant cause of the scalar plume intermittency, however without the spatial coherence. Finally, it must be noted while interpreting these snapshots that we are only measuring a single plane, and that we are limited to observing these coherent trends only when the coherent vortex packet is aligned with the measurement/injection plane.

6.2. *Statistical footprint with coherent vortex packets*

6.2.1. *Conditional structure for log injection*

Based on these qualitative observations, we can devise a statistical approach to investigate the dominance of these trends via conditional fields. However, since the conditional

averages require a large quantum of data, we estimate the same using the linear stochastic estimation approach previously employed to observe similar spatial trends (Adrian *et al.* 1989; Adrian 1994). The conditional field of a quantity $Q(\bar{x})$ conditioned on the occurrence of a second quantity ('event') $Q_E(\bar{x}_r)$ at reference location $\bar{x}_r$ is given as

$$\langle Q(\bar{x})|Q_E(\bar{x}_r)\rangle \approx \frac{\langle Q(\bar{x})Q_E(\bar{x}_r)\rangle}{\langle Q_E Q_E\rangle} Q_E(\bar{x}_r). \tag{6.1}$$

That is, the two-point correlation function embodies the information of the conditional field to first order, when conditioned on a single scalar quantity. Since the aforementioned coherent reorganisation was found consistently upstream when the scalar plume is transported far away from the injection location, we first choose this as the reference event, i.e. $\bar{x}_r = (2.75\delta, 0.3\delta \equiv h_i + 1\sigma_y)$ to estimate the concentration ($\langle \xi'(\bar{x})|\xi'(\bar{x}_r)\rangle$) and velocity fields $\langle \bar{u}(\bar{x})|\xi'(\bar{x}_r)\rangle$. This is shown in figure 17(*a*), that depicts the conditional concentration fluctuation and velocity fields in the field of view. A few aspects are immediately obvious from the conditional field. The correlation near the wall at $x \approx x_r$ reaches negative values, which implies that a high-concentration event away from the wall is accompanied by a low concentration close to the wall at the same streamwise location. This is expected for a conserved, meandering scalar. The conditional velocity fields around the reference location, $\bar{x}_r$, also exhibit a positive v' and negative u' (an 'ejection/Q2' event). This is entirely consistent with the turbulent flux at $\bar{x}_r$, discussed earlier in § 4. The most striking observation in the conditional scalar field is that a high-concentration event at $\bar{x}_r$ (we refer to this region of coherence as 'primary blob', P) is accompanied by two 'secondary blobs' of positive concentration fluctuation, upstream and closer to the wall (marked by S in figure 17*a*). The line joining these discrete, high-concentration regions is inclined at $\approx 10°$, consistent with the inclination angle of coherent vortex packets (Adrian *et al.* 2000*b*; Christensen & Adrian 2001; Adrian 2007). The robustness of these discrete secondary blobs is also observed in a statistically independent, but complementary measure in figure 17(*b*). Here the correlations for a positive concentration fluctuation in a region close to the wall, i.e. $\langle \xi'(\bar{x})|\xi'(\bar{x}_r)\rangle$ and $\langle \bar{u}(\bar{x})|\xi'(\bar{x}_r)\rangle$ with $\bar{x}_r = (2.75\delta, 0.04\delta)$, are shown. Not only does the anti-correlation at the outer location corresponding the primary concentration blob at $\bar{x} = (2.75\delta, 0.3\delta)$ appear (as expected), but we also see the anti-correlation blobs at the secondary locations ($\bar{x} \approx (1.95\delta, 0.18\delta)$ and $(1.6\delta, 0.1\delta)$) at exactly the same locations. This relative correlation structure by two independent measures demonstrates the robustness of this spatial organisation. Further, these observations are insensitive to the exact location of the $\bar{x}_r$ chosen, as long as it is in the vicinity of the primary blob seen here. Finally, the conditional structure in figure 17(*b*) indicates a consistent Q3 event (i.e. $u' < 0$, $v' < 0$) that is unusual to observe in a boundary layer. This structure appears in the relative frame as a pair of counter-rotating vortices, and demonstrates that the scalar below the injection location occurs predominantly in the low-momentum regions, indicating a strong relation with a UMZ. This observation was insensitive to the choice of x_r for all choices of $y_r < y_{inj}$.

If we were to hypothesise that this discrete spatial coherence in scalar concentration occurs due to the action of a coherent vortex packet, as was seen in figure 16, the same should be observable in the conditional estimates based on the occurrence of a swirl event, i.e. $\langle \xi'(\bar{x})|\lambda_{ci}(\bar{x}_r)\rangle$. A swirl event for $y_r > y_{inj}$ was found to generally have a positive mixture fraction, ξ', below–upstream and a negative concentration above–downstream of the reference location. This velocity–concentration field is consistent with that observed for a primary blob in figure 17(*a*). Thus to induce the primary scalar blob at the same location, i.e. $\bar{x} = (2.7\delta, 0.3\delta)$, a swirl event at $\bar{x}_r \approx (2.77\delta, 0.37\delta)$ is considered, as shown in figure 17(*c*). The typical signatures of a coherent vortex

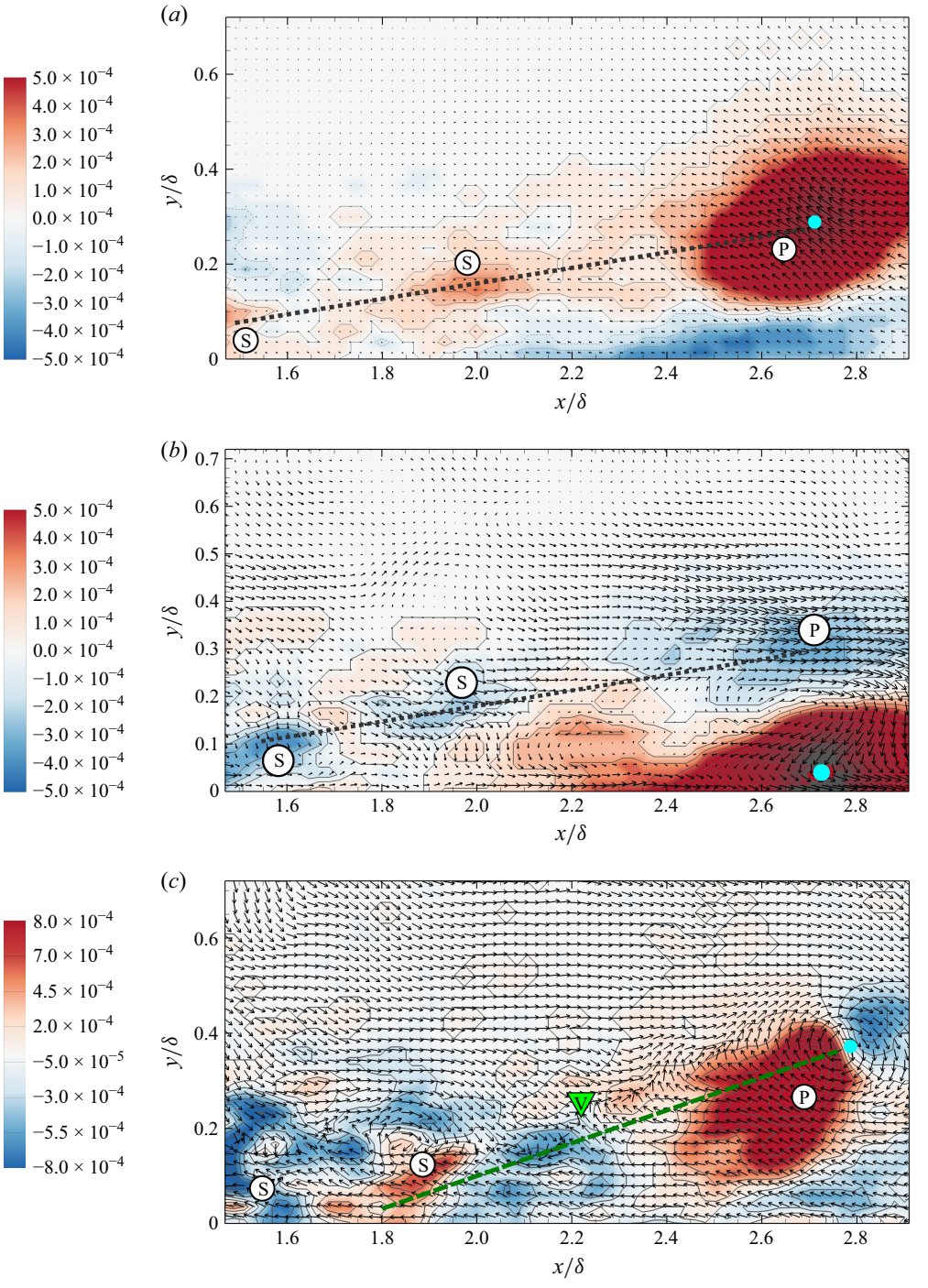

Figure 17. Conditional fields of scalar concentration perturbation and relative fluid velocity. (*a*,*b*) Conditioned on a positive scalar fluctuation and vectors show the velocity field. (*c*) Conditioned on a clockwise swirl event and vectors show velocity direction. Blue circles indicate the reference locations for each event.

packet (Adrian *et al.* 2000*b*; Christensen & Adrian 2001; Adrian 2007) in the conditional velocity field ($\langle\hat{u}(\bar{x})|\lambda_{ci}(\bar{x}_r = (2.77\delta, 0.37\delta))\rangle$) are reproduced accurately (for clarity, velocity direction $\langle\hat{u}|\lambda\rangle = \langle\bar{u}|\lambda_{ci}\rangle/|\langle\bar{u}|\lambda\rangle|$, with unit magnitude, is shown in figure 17*c*). Specifically, the primary hairpin head, and two 'younger', secondary hairpins appear with an inclined shear flow between them. Remarkably, the conditional scalar field shows the three positive peaks associated with the primary and secondary blobs at their respective locations identified in figure 17(*a*). This shows direct correlation between the coherent vortex packets and the scalar concentration blobs, as was hypothesised from instantaneous observations in figure 16(*a*,*b*). Additionally, the scalar blobs seem to be isolated from each other with influx events from the upstream vortex and a VITA event (saddle-point-like vector topology, marked V; Adrian 2007) that serve as topological barriers for the passive scalar. This provides a dynamical mechanism based on the coherent vortex packets for origination and development of discrete coherent scalar packets.

First, it must be noted that the evidence presented in figure 17(*a*,*b*) does not, by itself, substantiate the conclusion that the vortex packets are responsible for the coherent scalar arrangement. They only demonstrate that the scalar is distributed in discrete packets along an inclined line. This arrangement was found to be very robust and insensitive to the choice of x_r (for a similar y_r). The relation between the coherent vortices and the relative scalar field is seen only when a conditional swirl event is observed (figure 17*c*). As we present it here, the equivalence in the two observations is hypothesised only due to the compelling similarities in the two independent measures, and additional trends discussed in Appendix A. Additionally, we do not notice secondary swirl in the velocity fields conditioned on concentration event in figure 17(*a*,*b*). This could be because of a combination of the following factors:

(i) The advection of the high-concentration blob will dominate the velocity features observed in the conditional average, rather than the swirl and the long-range spatial coherence.

(ii) We expect a high-concentration blob to span a larger spanwise extent than the swirl field. This results in averaging over velocity features that are not in the symmetry plane, and in decreasing the long-range correlation of coherent vortices (dominant only in the symmetry plane). The swirl condition (figure 17*c*) does not suffer from this as it decays faster in the spanwise direction (due to hairpin shape) and the misaligned cases do not contribute to the correlation. Figure 17(*a*) represents an average that is agnostic to this distinction. We demonstrate via analysis presented in Appendix A that about 50 % of the concentration events occur coupled with a swirl event. A direct average conditioned on both events does elucidate a weak secondary swirl (in figure 22) coupled with a secondary concentration blob.

In addition to the primary blob as reference, we investigate the conditional fields based on the occurrence of a near-wall secondary blob, i.e. a discrete concentration event at a location $\bar{x}_r = (1.97\delta, 0.17\delta)$. This is shown in figure 18(*a*). No correlated downstream–outer peak in concentration representative of the earlier primary blob is observed, indicating that the concentration fluctuations at this location are not necessarily correlated with a coherent arrangement of concentration blobs (as was seen in figure 17*a*). This indicates that there are other mechanisms at play beyond that of a large attached, coherent vortex packet that discretise the injected stream of passive scalar into pockets at this location. In other words, an occurrence of a discrete blob at an injection location is not necessarily an indication of a coherent vortex packet. This is entirely consistent with qualitative observations made from the instantaneous snapshots where, on more occasions

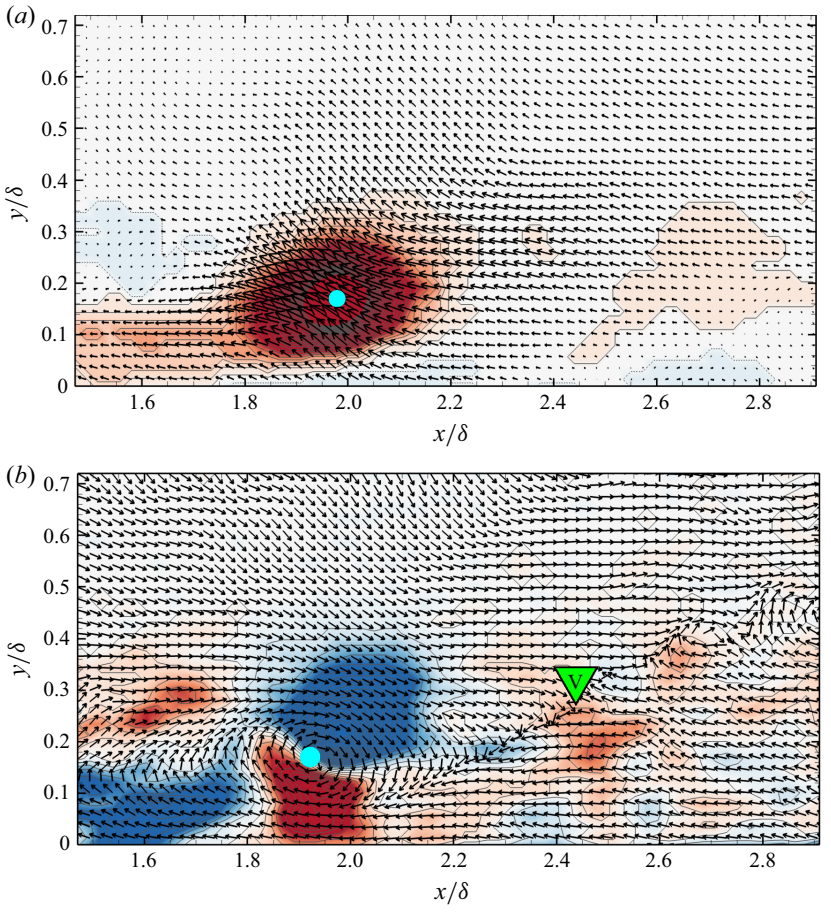

Figure 18. (*a*,*b*) Same as figure 17(*a*,*c*), but for a different reference location.

than not, a discrete scalar blob at the injection location is not accompanied by an inclined arrangement of coherent blobs. Finally, if we consider the occurrence of a vortex event ($\langle \xi'(\bar{x}) | \lambda_{ci}(\bar{x}_r) \rangle$) close to the wall instead of a concentration event ($\langle \xi'(\bar{x}) | \xi'(\bar{x}_r) \rangle$), we do see a corresponding coherent arrangement of discrete blobs along the inclined shear layer, as shown in figure 18(*b*). This definitively demonstrates the action of the coherent vortex packets in the discretisation and transport of the passive scalar along the shear layer. Finally, it is worth noting that the observations discussed here were insensitive to the exact values of $\bar{x}_r$ shown here, as long as they were in the same approximate regimes.

We can contextualise these observations with those observed in prior works that evaluated the large-scale structure associated with scalars (Antonia & Fulachier 1989; Metzger 2002; Laskari *et al.* 2020; Eisma *et al.* 2021). Specifically, the works established the conditional large-scale structure associated with 'coolings' (equivalently the trailing edge of a large, low-momentum bulge inclined in the streamwise direction). The works of Antonia & Fulachier (1989) established that these structures have a saddle-like topology in local turbulence, and Laskari *et al.* (2020) established the fine-scale structure of the same, demonstrating a smaller-scale vortex distribution. The role of these structures in a point-source injected scalar is perfectly demonstrated in the conditional fields (figure 17),

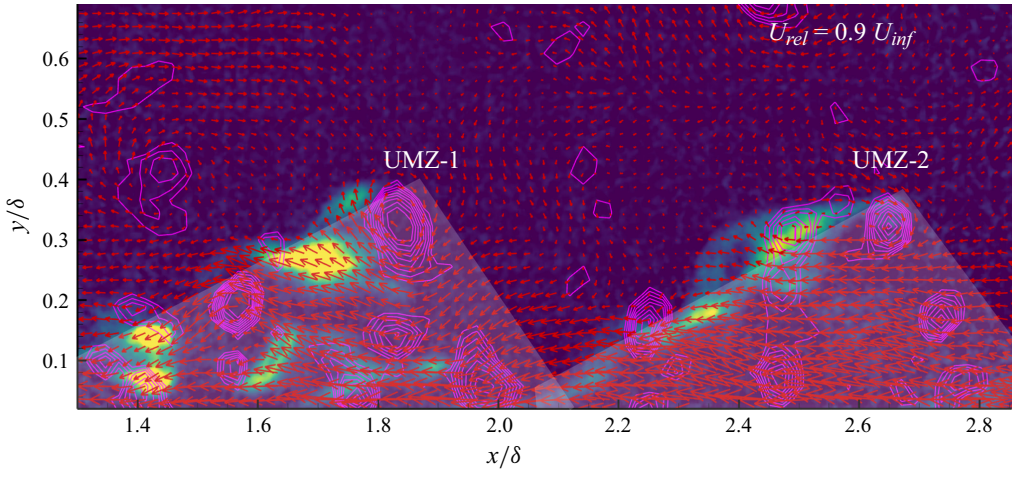

Figure 19. An illustrative snapshot qualitatively showing ramp-like UMZ features and relative arrangement of vortex packets and scalars. Velocity field shown relative to a moving frame of reference, $U_{rel} = 0.9U_\infty$. Magenta contours represent contours of high $|\lambda_{ci}|$, and scalar contours are the same as in figure 16.

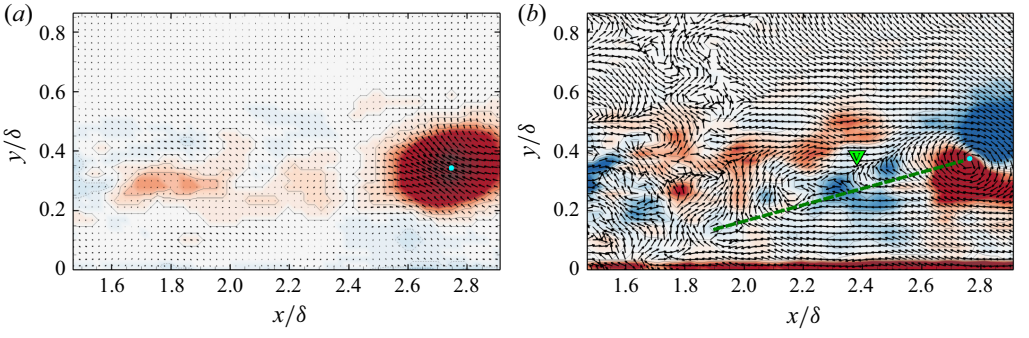

Figure 20. (*a*,*b*) Same as figure 17(*a*,*c*), but for wake injection.

and the illustrative instantaneous field shown in figure 19. This integrates the advection arguments of Antonia & Fulachier (1989) and Laskari *et al.* (2020), the coherent vortex packets (Adrian 2007) and the observance of these as UMZs. Specifically, the trailing edge of the UMZs represent the 'cooling' events (Antonia & Fulachier 1989), and the vortices arranged represent the finer structure observed in Laskari *et al.* (2020). Both these works use temperature as a proxy for low-momentum regions. The current work demonstrates that the injected scalar 'hitch-hikes' on the 'cooling events' resulting in a large meander event. In the process, the saddle-like topology induces the spatial discretisation observed both instantaneously (figure 19) and stochastically (figure 17*c*).

6.2.2. *Conditional structure for wake injection*

Similar conditional analysis can be performed when the scalar is injected into the wake region to see if any coherent trends of similar nature are observable. Figure 20(*a*) shows the conditional fields, $\langle \xi'(\bar{x})|\xi(\bar{x}_r)\rangle$ and $\langle \bar{u}(\bar{x})|\xi'(\bar{x}_r)\rangle$, where a $\xi' > 0$ event is observed slightly above the injection location ($\bar{x}_r = [2.75\delta, 0.35\delta]$). The meandering nature of the plume is evident, since the positive correlation at the reference location is accompanied by a negative correlation below the injection location. There also appears to be a secondary

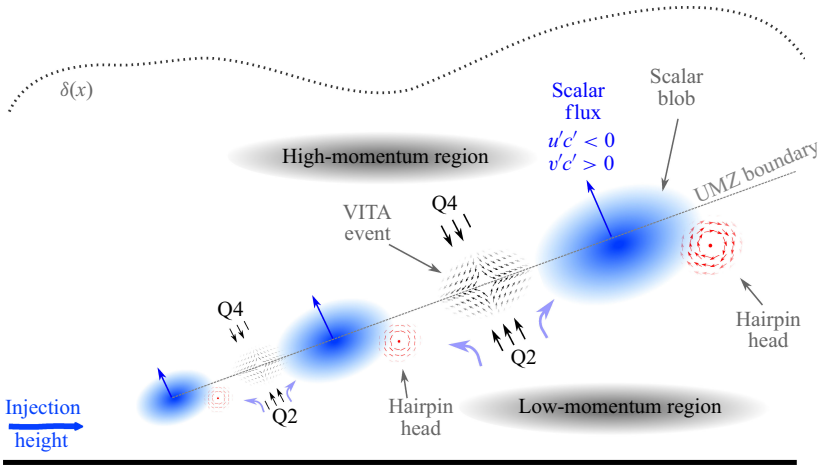

Figure 21. Schematic of meandering of the plume by the coherent vortex packet.

correlation peak upstream of the reference location along the injection line. This can be representative of mean separation distance of the discrete blobs. Further, recall from the instantaneous snapshots (figure 16) that discrete scalar blobs were consistently associated with vortices. This can also be observed in figure 20(*b*), where $\langle \xi'(\bar{x})|\lambda_{ci}(\bar{x}_r)\rangle$ and $\langle \hat{u}(\bar{x})|\lambda_{ci}(\bar{x}_r)\rangle$ fields are shown, with $\bar{x}_r = [2.75\delta, 0.35\delta]$. The swirl at $\bar{x}_r$ induces the ejection event $u' - v'$ seen in figure 20(*a*), and the relative ξ' field is also shown. The occurrence of a discrete concentration blob is clearly seen here, with a scalar-excess region ($\xi' > 0$) sandwiched between two scalar-deficit regions ($\xi' < 0$). The relative organisation of this ξ' structure with the inclined shear layer of the coherent vortex packet is also evident, with the VITA event (marked V) serving as a material barrier to the ejected plume. The sweep event from the secondary vortex upstream and along the shear layer (marked S) appears to play a dominant role in breaking up of the plume by bringing in the scalar-deficit free-stream fluid. Beyond this primary blob, the secondary blob seen in figure 20(*a*) does not appear in this vortex-conditioned field. However, the inclined shear layer that is characteristic of the coherent vortex packet does appear to direct the injected scalar plume away from the wall, while sustaining a concentration gradient normal to it. Beyond these two aspects, i.e. the breakup of the primary packet and the deflection of the upstream plume, the vortex packet does not seem to play a direct role in a coherent breakup and reorganisation of discrete scalar plumes as was observed in the case of log-region injection.

From these observations, we can make a phenomenological model for the scalar plume dispersal for both injection cases, as demonstrated in figure 21. When the scalar plume is injected in the logarithmic region, the role of turbulence in breaking up the plume into discrete pockets of varying sizes (discussed previously in § 5) can be viewed as a combination of two aspects – (i) an incoherent interaction of the plume with various vortical motions $\mathcal{O}(1\,\sigma_y, 1\,\sigma_z)$ and (ii) an interaction of the plume with a growing coherent vortex packet occurring near the wall. The former was not investigated in much detail in the current work. The interaction with the latter (itself a dominant dynamic process within a boundary layer) not only disperses the scalar plume into discrete coherent pockets, but also transports these away from the wall into the wake region together with the oldest/largest hairpin vortex. This appears to be the dominant mechanism by which the scalar plume can reach the outer extents of the boundary layer ($y/\delta > 0.4$) in relatively high concentrations.

This highlights the dominant role of the coherent vortex structures and a mechanistic transport mechanism of wall-normal transport of passive scalar close to the wall. On the other hand, when the scalar is injected in the wake region, the incoherent dispersal seems to be the dominant mechanism by which the scalar plume breaks up. The interaction with the vortex packet only occurs at larger, older vortices that are detached from the wall. The spatial coherence has only a weak interaction with the upstream plume, which appears as a slight wall-normal deflection of the plume along the inclined shear layer. This indicates that a purely statistical approach, such as a meandering plume model, can reasonably capture the scalar dispersal for a scalar injected in the wake region. Finally, it is important to note that this coherent viewpoint is only valid when the symmetry plane of the vortex packets is approximately aligned with the injection plane. They will have a role in spanwise meandering of the plume when there is a misalignment between the two planes, which is not investigated here. In other words, we are incorporating the influence of non-aligned vortex packets as the incoherent component in this paradigm. Measurements similar to these in the streamwise–wall-parallel plane might be best suited for these studies.

7. Discussion and conclusions

Implementing and validating the simultaneous planar velocity and quantitative mixture fraction measurements using synchronised PIV and Ac-PLIF, let us study the spatial aspects of the scalar plume evolution. Specifically, we focus on the region shortly downstream of the injection location ($1.5 \leqslant x/\delta \leqslant 3$) when the scalar is injected isokinetically in logarithmic and wake regions of the TBL. The plume behaviour is dominated by strong meandering and exhibits high intermittency in this region (Fackrell & Robins 1982*b*; Crimaldi *et al.* 2002). We particularly focused on the stochastic description here, that can leave a footprint in the evolution of the scalar at far downstream locations.

7.1. *On the mean plume evolution and plume spread*

Given the novelty in the diagnostic approach, especially for flows in air, we first quantified the canonical nature of the experiments using the mean plume evolution and single-point statistics ($\overline{\xi'^2}$, $\overline{u'\xi'}$, $\overline{v'\xi'}$). This also established the baseline behaviour. It was found that the Gaussian plume model captures the mean evolution well, with its spreading behaviour being reasonably captured by the analytical models (Nironi *et al.* 2015). Additionally, the meandering plume model (Gifford 1959; Marro *et al.* 2015) was also found to quantitatively capture the behaviour, as the instantaneous plume structure was found to only weakly depend on the wall-normal distance. Perhaps the most interesting discrepancy with previous work is with the angle of maximum two-point concentration correlation as compared with those measured by Talluru & Chauhan (2020). Our current measurements show a mean angle $\alpha \approx 70^\circ$ (figure 10), which is different from $\approx 30^\circ$ that was observed by Talluru & Chauhan (2020) for a similar x/δ, h_i/δ location (using two-probe measurements and Taylor's hypothesis). The streamwise extent for the correlations in the current work was also found to be smaller. Though the outer-scaled injection location, h_i/δ, is matched, there are differences in the relative source diameters (d_s/δ) and relative plume sizes (σ_y/δ) between the two efforts which can affect mean vorticity experienced by the plume. It appears that the boundary-layer scaling x/δ is not an appropriate scaling parameter to capture the streamwise variation of the angle (Miller 2005). A more focused study is required to understand the relevant evolution and scalings of these quantities.

7.2. *On the plume intermittency and breakup*

The plume behaviour is highly intermittent in the streamwise region of interest, with intermittency values $\gamma \approx 60\,\%$ similar to those observed in Crimaldi *et al.* (2002). The availability of the spatial information enabled us to explore this behaviour as 'blobs' of scalar plume as viewed in the plane of measurement. These blobs sustain locally high values of scalar concentration relative to the unconditional mean. Specifically, we looked at the shape, size, mean concentration and inclination of these conditional blobs. The distribution of the concentration and the blob size indicated that stretching–straining motions and the plume breakup due to large turbulent scales is the primary mode of plume evolution, and that there was very little small-scale scalar mixing. This was true for both injection locations, and can be explained by the relative absence of small-scale turbulence away from the wall compared with the buffer layer (Ng *et al.* 2011). Further, for both injection locations, the distribution of blob parameters did not significantly depend on the wall-normal distance from the injector. This further strengthens the meandering plume hypothesis, and shows that the plume has not had time to significantly adapt to local turbulent conditions at different wall-normal locations. Finally, the distribution of the blob inclination angle $\tilde{\phi}$ and the elongation $\widetilde{AR}$ show that they are inclined forward (downstream direction) and stretched by around 18 %. These observations bolster the trends observed previously by Talluru & Chauhan (2020). The inclination was slightly higher for the log-region injection compared with the wake-region injection due to the increased shear that the structures encounter as they meander away from the source.

7.3. *On the role of coherent vortices*

Investigation of scalar blobs relative to the turbulent structure indicated interesting patterns. Firstly, and unsurprisingly, it was observed that the swirling motions within the boundary layer are the primary mechanisms by which the plume meanders and breaks up within the boundary layer. The blobs exhibited a correlated arrangement with the swirling strength for both injection locations. This was particularly interesting given the existence of well-known coherent packets of hairpin vortices, that result in large-scale and very-large-scale motions. Upon a further investigation using linear stochastic estimations, the following coherent trends in scalar plume arrangement were observed:

(i) Along the line of injection (i.e. $y \sim h_i$), the scalar blobs were generated via the action of coherent and incoherent swirling motions, and the contributions from the former were not statistically significant to the overall scalar variance. This was true for both injection locations (log and wake).

(ii) However, plume interactions with a vortex that is a part of a coherent packet show a distinct footprint along the shear layer inclined at $\approx 10° - 15°$ (figure 17*c*). This demonstrated that the packets coherently organise the scalar plume. This is particularly dominant for the log-region injection, and was backed by multiple instantaneous realisations.

(iii) More importantly, this coherent mechanism was dominant and statistically significant when the scalar plume meanders away from the injection location significantly, especially for the log-region injection. In other words, when a scalar blob was observed at locations $y \gtrsim h_i + 1.5\sigma_y$, this was almost always associated with the action of a coherent packet. This was evidenced both from the conditional concentration fluctuation at this location and from the conditional vortex events (with their correlated concentration fields). We refer to this as the 'large meander event'.

(iv) The large meander event that is coupled with a coherent packet also showed a distinct spatial arrangement in plume structure. Specifically, a strong scalar blob meandering far away from the wall was seen to have correlated, secondary blobs along the shear layer associated with the secondary vortices of the vortex packet. This was observed only for the log-region injection where the injected plume interacts with the earlier generations of vortices close to the wall. The wake-region injection only interacts with larger, older generation of vortices and does not show this arrangement.

(v) Finally, the region between the scalar blobs was found to sustain, on average, a saddle-like vector topology, commonly known as a VITA event for the coherent vortex packet (Adrian *et al.* 2000*b*). The observed trends are highly consistent with those of Antonia & Fulachier (1989) and Laskari *et al.* (2020) who observed the structure of large-scale events.

Based on the above observations, we can propose a mechanistic paradigm (illustrated in figure 21) for the meandering of the scalar plume to add dynamical detail to that presented in Vanderwel & Tavoularis (2016), Talluru *et al.* (2018) and Eisma *et al.* (2021). When the plume is injected in the logarithmic region, it interacts with a range of vortices that cause it to meander in the spanwise and wall-normal directions. However, some of these vortices are part of a larger vortex packet that induce a coherent forcing of the plume. The plume appears to respond to this, and the meandering occurs in and out of the plane along the inclined shear layer. While this is not a statistically dominant meandering mechanism along the injection line (as was seen in § 5.1), this appears to be the primary mechanism by which the scalar plume reaches the outer regions of the boundary layer. This has important implications on the rare, strong-meander events, and provides a phenomenological explanation for the rare concentration fluctuations that occur far away from the injection location. Importantly, the current work demonstrates that a scalar from a point source gets transported along the inclined interface of the UMZs over large wall-normal distances (figure 19), while also being discretised in a spatially coherent manner by the action of the associated coherent vortex packets. A Lagrangian analysis of the coherent packet evolution will elucidate this paradigm more comprehensively. For a plume that is injected in the wake region, the coherent packet still appears to have a significant role in arranging the scalar into discrete blobs. This is particularly true as the blobs were found coherently placed with vortices. However, this was not found to be a dominant contributor of scalar variance at any wall-normal location, at least for the injection location considered in the current work. This is possibly due to the plume's interactions predominantly with older generations of vortices, some of which will be detached from the surface and lack spatial coherence.

In summary, the distribution of strong vortical motions within the boundary layer appears to have a disproportionate influence on the meandering and intermittency characteristics of a passive scalar plume, particularly close to the injection location. Coupled with their role in the sustenance of uniform concentration zones at further downstream locations (Eisma *et al.* 2021) and the correlation between the inclined shear layers and scalar gradients observed before (Laskari *et al.* 2020), the dynamical significance is clearly evident. Given the well-established scaling of these structures (Marusic & Monty 2019), it will be interesting to investigate how these translate into their role in passive scalar transport in atmospheric flows.

Acknowledgements. The authors are grateful for valuable insights from Professor R. Adrian on coherent structures.

Funding. The research was supported through a start-up grant provided by the Arizona State University.

Declaration of interests. The authors report no conflict of interest.

Author contributions. I.E.W. contributed by performing the experiments, implementing the diagnostics and analysis of all results in §§ 2–5. G.P. contributed analysis in § 6. Both authors contributed to the experiment conception, writing of the manuscript and the overall discussions.

Data availability statement. The data that support the findings of this study are available upon request.

Appendix A. An alternative heuristic measure of conditional structure

We present an alternative and independent perspective of the coherent scalar arrangement that is more intuitive than that presented in § 6, albeit being less rigorous, less converged and more subjective. This builds on the observations in instantaneous fields (figures 16 and 19), conditional-estimate fields (figure 17*a*,*c*) and the paradigm proposed (figure 21). We ask the question: given an approximate arrangement assumed between a large meander event and a swirl event, what would a relative conditional flow field be? For this, 'events' satisfying specific conditions were identified as follows (thresholds were based on the illustrative field in figure 16*a*):

(i) **Scalar event:** a large region ($\hat{A}_\xi > \hat{A}_t \approx (0.05\delta)^2$) of high concentration ($\xi > 0.22$) occurs away from the wall ($\hat{x},\ \hat{y} > 0.25\delta$). A total of $\hat{N}_\xi = 2347$ events were observed (out of the 2434 fields captured).

(ii) **Swirl event:** a large region ($\hat{A}_\lambda > \hat{A}_t \approx (0.05\delta)^2$) of high clockwise swirl ($\lambda_{ci} < -675\delta/U_{inf}$) occurs away from the wall ($\hat{N}_\lambda = 11\,477$ events in total).

(iii) **Paired events:** subsets of these two events, where they occur simultaneously with the following arrangement, were extracted:

   (*a*) The swirl event occurs downstream and above the concentration event (marked using area centroids), with a minimum separation of 0.01δ in x and y directions.

   (*b*) The swirl event occurs within a maximum distance, $\hat{\Delta} < 0.21\delta$.

   In occasional cases where multiple swirl events satisfy this proximity criterion, the swirl event nearest to the scalar event is considered. This identified $\hat{N}_P = 1205$ pairs in the 2434 fields captured.

This identification and detection method is illustrated in figure 22. The number of detected events implies that there were, on average, 0.495 such pairs per measured field. More crucially, there is a 51.3 % probability that a large concentration event is simultaneously accompanied by a large and strong swirl event downstream–above it and within the vicinity chosen.

For all these 'paired events', the spatial neighbourhoods were extracted and conditionally averaged, to get the relative turbulence field and ξ' field (from the frame of reference of the swirl event). The conditional averaged fields are shown in figure 22(*b*). Note that there was no distinction made for paired events occurring at different x and y locations (except for the $\hat{y}$ threshold). For this reason, the conditional field close to the wall will be averaged across multiple wall-normal locations. This means that the near-wall structure observed in these fields will differ from that discussed in § 6. The conditional structure demonstrates many of the same features identified in figure 17(*c*). The primary swirl–blob coupling is due to the choice of the conditional field. However, a weak secondary peak also appears coupled to a weak swirl, together with an inclined region of negative $\hat{\xi}'$. The indiscriminate nature of this direct conditional averaging, where

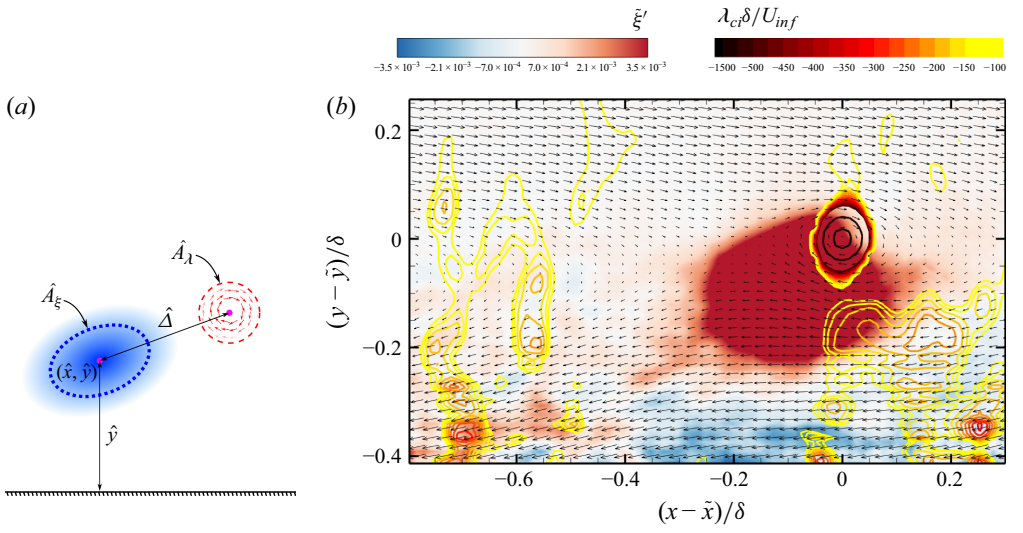

Figure 22. (*a*) Schematic representation of the conditional event chosen. (*b*) Conditional average of concentration fluctuation, velocity and swirl fields of the detected events (log-injection case). Swirl contours are chosen to de-emphasise the conditional event (large swirl) and emphasise the secondary features.

multiple packets at different wall-normal distances are averaged, and limited convergence erodes the finer features observed in figures 17(*c*) at large distances from reference location. Despite this, the sustenance of primary and secondary blobs, their relative arrangement and the fact that ≈50 % of high-concentration blobs occur with a swirl event in close vicinity provide additional statistical evidence to the coupling between the coherent vortex packets and large scalar wall-normal meander.

References

Adrian, R.J. 1994 Stochastic estimation of conditional structure: a review. *Appl. Sci. Res.* **53** (3–4), 291–303.

Adrian, R.J. 2007 Hairpin vortex organization in wall turbulence. *Phys. Fluids* **19** (4), 041301.

Adrian, R.J., Christensen, K.T. & Liu, Z.-C. 2000*a* Analysis and interpretation of instantaneous turbulent velocity fields. *Exp. Fluids* **29** (3), 275–290.

Adrian, R.J., Jones, B.G., Chung, M.K., Hassan, Y., Nithianandan, C.K. & Tung, A.T.-C. 1989 Approximation of turbulent conditional averages by stochastic estimation. *Phys. Fluids A: Fluid Dyn.* **1** (6), 992–998.

Adrian, R.J., Meinhart, C.D. & Tomkins, C.D. 2000*b* Vortex organization in the outer region of the turbulent boundary layer. *J. Fluid Mech.* **422**, 1–54.

Antonia, R.A. & Fulachier, L. 1989 Topology of a turbulent boundary layer with and without wall suction. *J. Fluid Mech.* **198** (-1), 429.

Buch, K.A. & Dahm, W.J.A. 1996 Experimental study of the fine-scale structure of conserved scalar mixing in turbulent shear flows. Part 1. Sc [Gt] 1. *J. Fluid Mech.* **317**, 21–71.

Buch, K.A. & Dahm, W.J.A. 1998 Experimental study of the fine-scale structure of conserved scalar mixing in turbulent shear flows. Part 2. *Sc*, ≈1. *J. Fluid Mech.* **364**, 1–29.

Cassiani, M., Ardeshiri, H., Pisso, I., Salizzoni, P., Marro, M., Stohl, A., Stebel, K. & Park, S.Y. 2024 The dynamics of concentration fluctuations within passive scalar plumes in a turbulent neutral boundary layer. *J. Fluid Mech.* **1001** (December), A18.

Cassiani, M., Bertagni, M.B., Marro, M. & Salizzoni, P. 2020 *Concentration Fluctuations From Localized Atmospheric Releases*. Boundary-Layer Meteorology.

Chakraborty, P., Balachandar, S. & Adrian, R.J. 2005 On the relationships between local vortex identification schemes. *J. Fluid Mech.* **535**, 189–214.

Chauhan, K.A., Monkewitz, P.A. & Nagib, H.M. 2009 Criteria for assessing experiments in zero pressure gradient boundary layers. *Fluid Dyn. Res.* **41** (2), 021404.

CHRISTENSEN, K.T. & ADRIAN, R.J. 2001 Statistical evidence of hairpin vortex packets in wall turbulence. *J. Fluid Mech.* **431**, 433–443.
CONNOR, E.G., MCHUGH, M.K. & CRIMALDI, J.P. 2018 Quantification of airborne odor plumes using planar laser-induced fluorescence. *Exp. Fluids* **59** (9), 137.
CRIMALDI, J.P. 2008 Planar laser induced fluorescence in aqueous flows. *Exp. Fluids* **44** (6), 851–863.
CRIMALDI, J.P. & KOSEFF, J.R. 2001 High-resolution measurements of the spatial and temporal scalar structure of a turbulent plume. *Exp. Fluids* **31** (1), 90–102.
CRIMALDI, J.P., WILEY, M.B. & KOSEFF, J.R. 2002 The relationship between mean and instantaneous structure in turbulent passive scalar plumes. *J. Turbul.* **3**, N14.
DHARMARATHNE, S., TUTKUN, M., ARAYA, G. & CASTILLO, L. 2016 Structures of scalar transport in a turbulent channel. *Eur. J. Mech. - B/Fluids* **55**, 259–271.
EISMA, J., WESTERWEEL, J. & VAN DE WATER, W. 2021 Do coherent structures organize scalar mixing in a turbulent boundary layer? *J. Fluid Mech.* **929**, A14.
FACKRELL, J.E. & ROBINS, A.G. 1982*a* Concentration fluctuations and fluxes in plumes from point sources in a turbulent boundary layer. *J. Fluid Mech.* **117**, 1–26.
FACKRELL, J.E. & ROBINS, A.G. 1982*b* The effects of source size on concentration fluctuations in plumes. *Boundary-Layer Meteorol.* **22** (3), 335–350.
FERNANDO, H.J.S., ZAJIC, D., DI SABATINO, S., DIMITROVA, R., HEDQUIST, B. & DALLMAN, A. 2010 Flow, turbulence, and pollutant dispersion in urban atmospheres. *Phys. Fluids* **22** (5), 051301.
GANAPATHISUBRAMANI, B., HUTCHINS, N., HAMBLETON, W.T., LONGMIRE, E.K. & MARUSIC, I. 2005 Investigation of large-scale coherence in a turbulent boundary layer using two-point correlations. *J. Fluid Mech.* **524**, 57–80.
GANAPATHISUBRAMANI, B., LONGMIRE, E.K. & MARUSIC, I. 2003 Characteristics of vortex packets in turbulent boundary layers. *J. Fluid Mech.* **478**, 35–46.
GIFFORD, F. 1959 Statistical properties of a fluctuating plume dispersion model. In *Advances in Geophysics*, vol. 6, pp. 117–137. Elsevier.
KLINE, S.J., REYNOLDS, W.C., SCHRAUB, F.A. & RUNSTADLER, P.W. 1967 The structure of turbulent boundary layers. *J. Fluid Mech.* **30** (4), 741–773.
LASKARI, A., SAXTON-FOX, T. & MCKEON, B.J. 2020 Spatial organisation of velocity structures for large passive scalar gradients. *J. Fluid Mech.* **885**, A33.
LIAO, Q. & COWEN, E.A. 2002 The information content of a scalar plume – a plume tracing perspective. *Environ. Fluid Mech.* **2** (1), 9–34.
LIM, H.D. & VANDERWEL, C. 2023 Turbulent dispersion of a passive scalar in a smooth-wall turbulent boundary layer. *J. Fluid Mech.* **969** (August), A26.
MARRO, M., NIRONI, C., SALIZZONI, P. & SOULHAC, L. 2015 Dispersion of a passive scalar fluctuating plume in a turbulent boundary layer. Part II: analytical modelling. *Boundary-Layer Meteorol.* **156** (3), 447–469.
MARRO, M., SALIZZONI, P., SOULHAC, L. & CASSIANI, M. 2018 Dispersion of a passive scalar fluctuating plume in a turbulent boundary layer. Part III: stochastic modelling. *Boundary-Layer Meteorol.* **167** (3), 349–369.
MARUSIC, I. & MONTY, J.P. 2019 Attached eddy model of wall turbulence. *Annu. Rev. Fluid Mech.* **51** (1), 49–74.
MATLAB R2023b. 2023 regionprops - Measure properties of image regions. The MathWorks Inc.
METZGER, M.M. 2002 Scalar dispersion in high Reynolds number turbulent boundary layers. PhD thesis, The University of Utah, United States – Utah.
MILLER, R.J. 2005 A study of passive scalar mixing in turbulent boundary layers using multipoint correlators. Thesis, Georgia Institute of Technology.
NATRAJAN, V.K. & CHRISTENSEN, K.T. 2006 The role of coherent structures in subgrid-scale energy transfer within the log layer of wall turbulence. *Phys. Fluids* **18** (6), 065104.
NG, H.C.H., MONTY, J.P., HUTCHINS, N., CHONG, M.S. & MARUSIC, I. 2011 Comparison of turbulent channel and pipe flows with varying Reynolds number. *Exp. Fluids* **51** (5), 1261–1281.
NIRONI, C., SALIZZONI, P., MARRO, M., MEJEAN, P., GROSJEAN, N. & SOULHAC, L. 2015 Dispersion of a passive scalar fluctuating plume in a turbulent boundary layer. Part I: velocity and concentration measurements. *Boundary-Layer Meteorol.* **156** (3), 415–446.
POREH, M. & CERMAK, J.E. 1964 Study of diffusion from a line source in a turbulent boundary layer. *Intl J. Heat Mass Trans.* **7** (10), 1083–1095.
ROBINSON, S.K. 1991 Coherent motions in the turbulent boundary layer. *Annu. Rev. Fluid Mech.* **23**, 601–639.
SALESKY, S.T. & ANDERSON, W. 2020 Coherent structures modulate atmospheric surface layer flux-gradient relationships. *Phys. Rev. Lett.* **125** (12), 124501.

SAWFORD, B.L., FROST, C.C. & ALLAN, T.C. 1985 Atmospheric boundary-layer measurements of concentration statistics from isolated and multiple sources. *Boundary-Layer Meteorol.* **31** (3), 249–268.

SAWFORD, B.L. & HUNT, J.C.R. 1986 Effects of turbulence structure, molecular diffusion and source size on scalar fluctuations in homogeneous turbulence. *J. Fluid Mech.* **165**, 373.

TALLURU, K.M. & CHAUHAN, K.A. 2020 Structural inclination angle of near-field scalar fluctuations in a turbulent boundary layer. *Intl J. Heat Fluid Flow* **81**, 108521.

TALLURU, K.M., HERNANDEZ-SILVA, C., PHILIP, J. & CHAUHAN, K.A. 2017 Measurements of scalar released from point sources in a turbulent boundary layer. *Meas. Sci. Technol.* **28** (5), 055801.

TALLURU, K.M., PHILIP, J. & CHAUHAN, K.A. 2018 Local transport of passive scalar released from a point source in a turbulent boundary layer. *J. Fluid Mech.* **846**, 292–317.

TALLURU, K.M., PHILIP, J. & CHAUHAN, K.A. 2019 Self-similar spectra of point-source scalar plumes in a turbulent boundary layer. *J. Fluid Mech.* **870**, 698–717.

TAVOULARIS, S. & CORRSIN, S. 1981 Experiments in nearly homogenous turbulent shear flow with a uniform mean temperature gradient. Part 1. *J. Fluid Mech.* **104**, 311–347.

THEODORSEN, T. 1952 Mechanisms of turbulence. In *Proceedings of the 2<Nd> Midwestern Conference on Fluid Mechanics*, *1952*.

TOWNSEND, A.A.R. 1976 *The Structure of Turbulent Shear Flow*. Cambridge University Press.

VANDERWEL, C. & TAVOULARIS, S. 2014 Measurements of turbulent diffusion in uniformly sheared flow. *J. Fluid Mech.* **754**, 488–514.

VANDERWEL, C. & TAVOULARIS, S. 2016 Scalar dispersion by coherent structures in uniformly sheared flow generated in a water tunnel. *J. Turbul.* **17** (7), 633–650.

VOLINO, R.J., SCHULTZ, M.P. & FLACK, K.A. 2007 Turbulence structure in rough- and smooth-wall boundary layers. *J. Fluid Mech.* **592**, 263–293.

WU, Y. & CHRISTENSEN, K.T. 2007 Outer-layer similarity in the presence of a practical rough-wall topography. *Phys. Fluids* **19** (8), 085108.

YEE, E., GAILIS, R.M. & WILSON, D.J. 2003 The interference of higher-order statistics of the concentration field produced by two point sources according to a generalized fluctuating plume model. *Boundary-Layer Meteorol.* **106** (2), 297–348.

YEE, E., KOSTENIUK, P.R., CHANDLER, G.M., BILTOFT, C.A. & BOWERS, J.F. 1993*a* Statistical characteristics of concentration fluctuations in dispersing plumes in the atmospheric surface layer. *Boundary-Layer Meteorol.* **65** (1), 69–109.

YEE, E., WILSON, D.J. & ZELT, B.W. 1993*b* Probability distributions of concentration fluctuations of a weakly diffusive passive plume in a turbulent boundary layer. *Boundary-Layer Meteorol.* **64** (4), 321–354.